POLITECNICO DI TORINO

Department of Mechanical and Aerospace Engineering (DIMEAS)

Master's Degree Thesis in Aerospace Engineering

Study and analysis of energy-optimal pointing manoeuvres for an astrometric space telescope with exoplanet detection purposes

Politecnico di Torino

INAF
ISTITUTO NAZIONALE DI ASTROFISICA

Supervisors
Prof. Lorenzo Casalino
Dr. Alberto Riva
Co-supervisors
Dr. Mario Gai
Dr. Deborah Busonero

Candidate
Chiara Scandaglia

Academic Year 2023/2024

Acknowledgements

I would like to profoundly thank Professor Lorenzo Casalino for giving me the opportunity to work on this thesis, showing great helpfulness right from the start. His guidance and feedback have been fundamental to the success of this work.

My heartfelt thanks go to Dr. Alberto Riva and the entire research team at the Astrophysical Observatory of Turin, who immediately welcomed me as one of their own and allowed me to work on this thesis in the best context I could imagine. Without their availability, expertise and constantly positive attitude, the completion of this work would have been extremely more difficult.

A big thank you to the friends I have made over the years and the wonderful memories they have helped me to build. Each and every one of you has given me something and has helped make me the person I am, and who perhaps until recently did not even think of finishing this journey.

Never enough thanks to Sem for giving me the inestimable honour of being at his side, with his ability to breathe new life into each day that I find myself facing.

The warmest thanks go to my parents for their unconditional support, even in the darkest moments. It is you who are largely responsible for why I am here now. Thank you very much for always believing in me, even when I myself was not able to. Thanks also to my dummy brother, if only to give me the chance to reinvent myself in the film industry in case my engineering career goes wrong...

And finally, a never too fond thank you to my grandparents for the wonderful life they have allowed me to grow into.

Thank you all from the bottom of my heart. These years of study have been such a ride, and I feel deeply privileged to have experienced it with you.

Abstract

The search for extrasolar planets is a fundamental resource for expanding our understanding of the Universe and investigating the likelihood that other worlds might harbour life. Among the several approaches employed for this purpose, the astrometric method offers significant advantages, as it provides an accurate estimate of the mass of the planet under consideration, which is not required to be necessarily aligned with the line of sight of the observer as for the transit or radial velocity techniques.

This thesis aims at analysing and simulating the pointing manoeuvres required by a future spacecraft carrying an optical instrument such as **RAFTER** (*Ring Astrometric Field Telescope for Exoplanets and Relativity*) to properly fulfil the objectives of an exoplanet astrometric search mission whilst minimizing the associated energy cost. RAFTER is an annular field telescope conceived and proposed with the goal of achieving consistent optical response over a wide field of view, which exhibits a compact and scalable design and enforces circular symmetry for each optical element.

Following an outline of the scientific case under scrutiny and a thorough dissertation of the theoretical aspects covered, the present work introduces the potential configurations selected for the satellite and an overview of the mission it shall undertake, with a particular focus on the field-of-view shift manoeuvres evaluated in this study. Subsequently, the mathematical model addressing the dynamics of the system and the optimal control problem implemented to simulate the manoeuvres at stake are detailed. Finally, the results obtained are provided and discussed.

List of Figures

List of Tables

Contents

Chapter 1

Introduction

Ever since the discovery of the first exoplanet, the search for worlds outside our Solar System has proved to be one of the most compelling and daring challenges in the field of astronomy, an essential tool for shedding light on the still numerous mysteries of the Universe. The by now countless extrasolar planets detected over the last few decades have opened up new avenues for the study of extraterrestrial life and greatly enriched our knowledge of the origin and evolution of planetary systems[2], as well as stimulating the common imagination with renewed concepts of exploration and conquest of the unknown.

One of the earliest and, theoretically, most effective methods for detecting exoplanets is the astrometric method. It is based on the precise measurement of the path followed by the star under observation, generated by a combination of the proper motion of the celestial body along its orbit around the centre of the Galaxy and the apparent parallax motion resulting from the revolution of the Earth around the Sun. The composition of these two motions generates a helicoidal trajectory which, if irregular and thus perturbed, reveals the presence of a 'unseen companion'; a significantly massive planet that, together with its parent star, orbits a common centre of mass. It is therefore evident how this method has the advantage, firstly, of providing a substantially exact estimate of the mass of the planet under scrutiny, and also, unlike the better known and more widely exploited transit and radial velocity methods, of extending its field of application to all those planetary systems that do not orbit in a plane aligned with the line of sight of the observer.[18, 19] In practice, what makes the application of this method exceptionally complex is the difficulty, at present, of achieving sufficient accuracy to identify the position displacement of a star caused by the presence of planets in orbit with it. As of 2023, the astrometric method has led to the discovery of only three Jovian planets, and obtaining high-accuracy astrometry remains a topic of significant research interest in the field,[2] primarily with a view to future research and detection of smaller, Earth-like planets.

A number of optical instrument concepts have been developed to address this goal. Among them, RAFTER (*Ring Astrometric Field Telescope for Exoplanets and Relativity*) is an annular field telescope proposed with the aim of achieving accurate astrometric performance over a wide field of view, preserving circular symmetry at the level of each optical element down to the focal plane, and thus obtaining a consistent optical response[11, 10]. The idea behind the observations is to measure the arc of the circle, and thus the angular distance, between the target star and a suitable reference star in the field of view[10]. The conceptual design of RAFTER is based on a compact 1 m diameter telescope, which is suitable for medium-class space observatories, but can be easily scaled and miniaturized to be implemented on a CubeSat[11].

The purpose of this thesis is to examine and evaluate the pointing manoeuvres that a spacecraft carrying the RAFTER optical instrument shall execute in order to successfully

accomplish an astrometric mission for exoplanet detection.

The successive five Chapters are organized as follows:

- Chapter 2 provides an insight into the scientific case study and introduces the features of the RAFTER optical instrument concept;
- Chapter 3 offers the theoretical fundamentals of satellite attitude dynamics and optimal control theory;
- Chapter 4 firstly presents the potential configurations selected for the satellite and an overview of the mission it shall undertake, with a particular focus on the field-of-view shift manoeuvres that will be simulated in this study, and subsequently it details the mathematical model and optimal control problem implemented to simulate the manoeuvres under consideration;
- in Chapter 5, the results obtained are provided and discussed;
- finally, in Chapter 6, the conclusions of the study are drawn.

Chapter 2

Scientific context of the study

The objective of this Chapter is to present the scientific context within which this thesis has been carried out. The initial section will provide a comprehensive overview of the rationale behind the search for exoplanets and introduce the most commonly employed methodologies in this regard. Thereafter, particular attention will be devoted to the astrometric method, highlighting its defining characteristics, the principal challenges it faces, and the current state-of-the-art implementations. Finally, a significant focus will be given to the RAFTER optical instrument concept and its performances during scientific operations.

2.1 Exoplanet detection: an overview

2.1.1 Definitions and background

An exoplanet is defined as a planet situated outside the Solar System, namely orbiting a star other than the Sun.

Following the first discovery of a giant Jovian planet around a *main sequence* Sun-like star in 1995, the search for exoplanets has turned out to be an interdisciplinary and trendsetting challenge, which, in addition to being a crucial means of paving new paths in the study of planetary systems, has consistently been intertwined with the need to address the age-old question of whether life exists beyond Earth. Such an ambitious and unprecedented pursuit has served as a compass for significant progress in this field.[20]

The continuous expansion of our understanding is propelled by the synergistic use of space-borne and ground-based technologies - such as adaptive optics and high precision spectrographs - to reveal the diverse array of planetary system structures present in our Galaxy[20, 2]. A number of space missions have been developed in recent years with the primary objective of detecting extrasolar planets, such as Kepler, CoRoT and TESS, which have emerged as fundamental for the advancement of research in the field.

By the end of 2023, the presence of more than 5500 planets had been established[2].

2.1.2 Planetary systems and types of exoplanets

On average, there is typically one planet per star[21], with around 20% of Sun-like stars harboring an "Earth-sized" planet within the habitable zone[22]. The majority of known exoplanets revolve around Sun-like stars, such as main-sequence stars falling under spectral classes F, G, or K[23] (see Figure 2.1 for reference).

A multitude of criteria have been employed to categorize the large number of exoplanet types, including those based on mass, size, and chemical composition. Table 2.1 provides

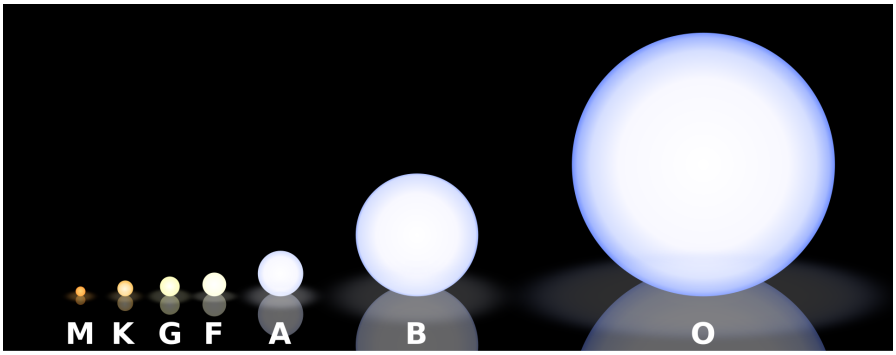

Figure 2.1: Morgan-Keenan spectral classification.[1]

an overview of these classifications, while Figure 2.2 illustrates a proposed division of exoplanets on the basis of the mass of the planets in the Solar System.[2]

Factor	Planet type	Parameter
Size	Earth size	1.25R - 2R
	Super Earth size	2R - 6R
	Jupiter size	6R - 15R
Mass	Earth	0.1M - 2M
	Sub Earth	10^{-8}M - 0.1M
	Super Earth	2M - 10M
	Neptunes	10M - 100M
	Jupiters	100M - 10^3M
	Super Jupiters	10^3M - $13M_J$
	Brown Dwarfs	$13M_J$ - $0.07M_S$
	Stellar Companions	$0.07M_S$ - $1M_S$
Composition (stellar flux)	Hot super Earths	187 - 1.12
	Warm Super Earths	1.12 - 0.30
	Cold super Earth	0.30 - 0.0030
	Hot Rocky	182 - 1.0
	Warm Rocky	1.0 - 0.28
	Cold Rocky	0.28 - 0.0035
	Hot Sub Neptunes	188 - 1.15
	Warm Sub Neptunes	1.15 - 0.32
	Cold Sub Neptunes	0.32 - 0.0.0030
	Hot Sub Jovians	220 - 1.65
	Warm Sub Jovians	1.65 - 0.45
	Cold Sub Jovians	0.45 - 0.0030
	Hot Jovians	220 - 1.65
	Warm Jovians	1.65 - 0.40
	Cold Jovians	0.40 - 0.0025

Table 2.1: Classification of exoplanets based on mass, size and chemical compositions of known gases such as ZnS, H_2O, CO_2 and CH_4.[2] R represents the radius of the Earth, M the mass of the Earth, M_J the mass of Jupiter and M_S the mass of the Sun.

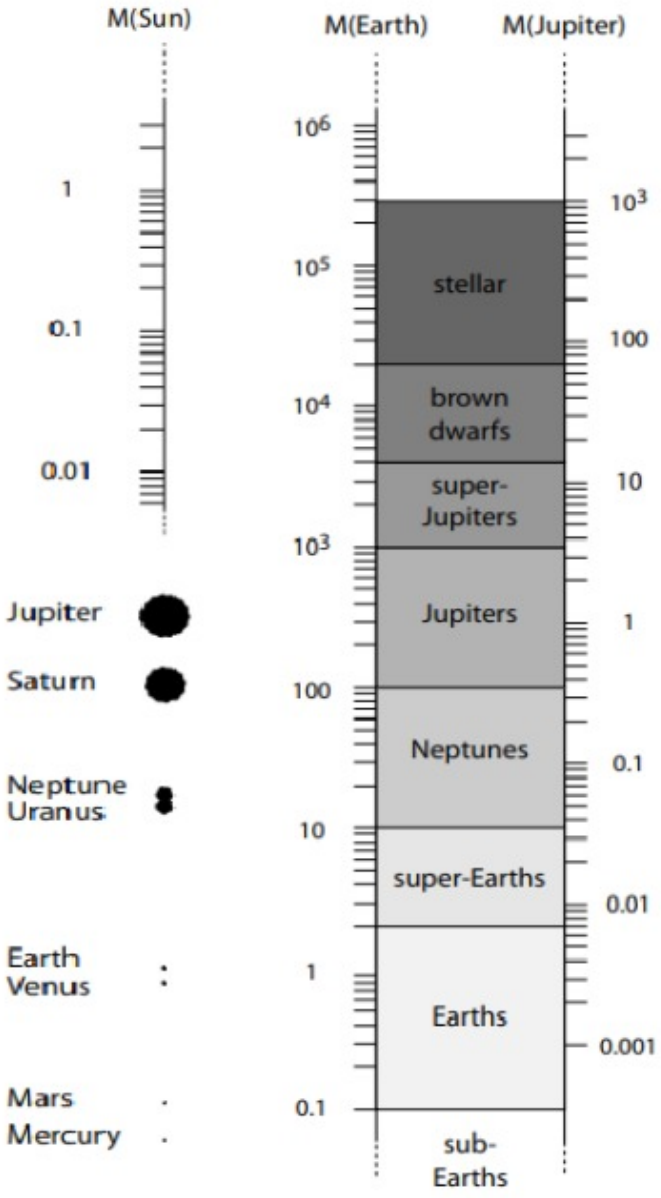

Figure 2.2: Planet masses categorized based on solar system objects[2].

2.1.3 Exoplanet detection purposes

As previously stated in this section, the study and discovery of planets outside our Solar System has not only illuminated new insights into the formation and evolution of planetary systems - often an observed exoplanet system could be at a very different stage than the Solar System, constituting 'time snapshots' of the various life stages of a planetary system - but also provided new and hitherto unimaginable means to understand and potentially detect traces of life in the remote corners of our Galaxy.

More in detail, planets are believed to come into existence relatively quickly after the formation of their parent star, typically within a span ranging from a few million to tens of millions of years.[24, 25] While we can only directly observe the planets within our own Solar System in their current state, studying diverse planetary systems of various ages

enables us to witness planets at different developmental phases. This includes observations of young proto-planetary disks where planets are still in the process of formation[26, 27], as well as mature planetary systems that have been in existence for over 10 billion years.

Concurrently, the other main objective of exoplanetary science is to detect traces of extraterrestrial life by unambiguously identifying biogenic gases and molecules in the air of a Earth-like orbiting a solar-type star.[20] More clearly, it should be emphasised that, at vast cosmic distances, the presence of life can only be identified if it has evolved on a planetary scale and significantly altered the planetary environment in a manner that cannot be attributed to conventional physico-chemical processes (non-equilibrium processes)[28]. For instance, the occurrence of molecular oxygen (O_2) in the Earth atmosphere is a consequence of photosynthesis carried out by living organisms such as plants and various types of microorganisms, making it a potential indicator of life on exoplanets, despite the possibility of non-biological sources producing small quantities of oxygen as well.[29]

Moreover, a planet that could potentially support life must revolve around a stable star at a distance that allows planetary-mass objects to maintain sufficient atmospheric pressure for the presence of liquid water on their surfaces.[30]

Habitable zone

The circumstellar **habitable zone** is the area surrounding a star where conditions are suitable for the presence of liquid water on the surface of a planet. This region is characterized by being located at an optimal distance from the star, preventing water from either evaporating due to proximity or freezing due to distance. The level of heat emitted by stars can vary based on factors such as size and age, resulting in different habitable zone distances for each star. Furthermore, the composition of the atmosphere of a planet plays a significant role in regulating heat retention, thus influencing the specific location of the habitable zone. For instance, desert planets, which are low in water content, exhibit reduced greenhouse effects compared to Earth, allowing for the possibility of water oases closer to their respective stars.[31] Conversely, rocky planets with dense hydrogen atmospheres can support surface water at distances exceeding that of Earth's orbit around the Sun.[32] Additionally, planets with greater mass possess wider habitable zones due to the impact of gravity on reducing the greenhouse effect of the water vapor, consequently shifting the inner boundary of the habitable zone closer to the star.[30] Figure 2.3 displays the habitable zones of different types of stars.[2]

2.1.4 Exoplanet detection methods

Numerous techniques for the detection of exoplanets have been developed and have made significant advances in the search for and study of extrasolar planets. This paragraph will examine the **transit method**, the **radial velocity** (or Doppler spectroscopy) method, the **gravitational microlensing** and the **direct imaging**. The following Section (2.2) will focus on the **astrometric method**, which forms the basis of the scientific observations of RAFTER.

Transit photometry

It is one of the most prolific methods of detecting exoplanets. It is based on the decrease in the brightness of a star that is observed when a planet transits in front of its disk, whose magnitude depends on the size of the star and the planet itself.[33, 34, 2] Figure 2.4 presents a graphical illustration of the periodic dips in brightness observed on the star TRAPPIST-1, corresponding to the transit of the planets in its planetary system.[35]

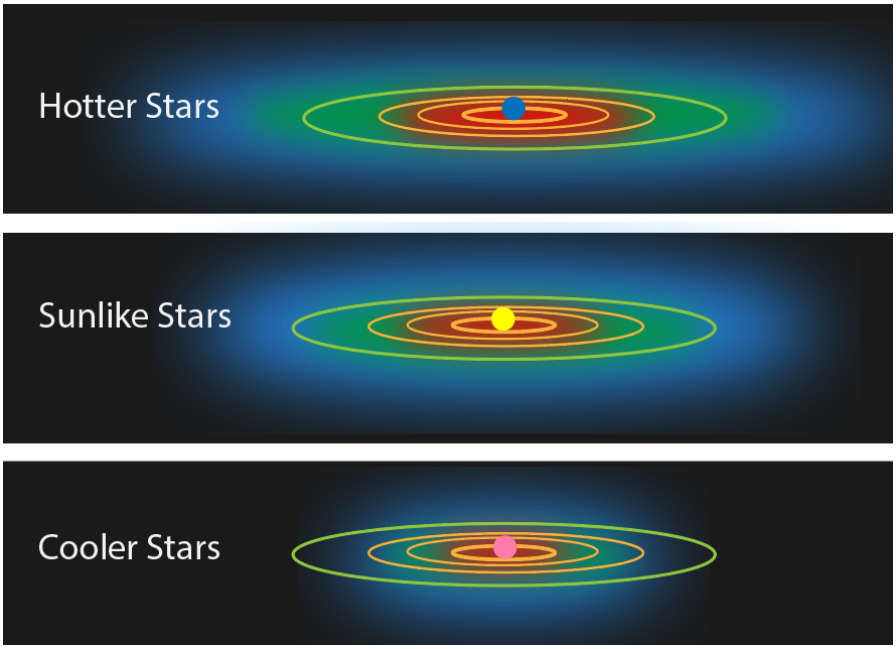

Figure 2.3: Habitable zones (in green) surrounding different types of stars. The red area is too hot, while the blue area is too cool to accommodate water in its liquid state.

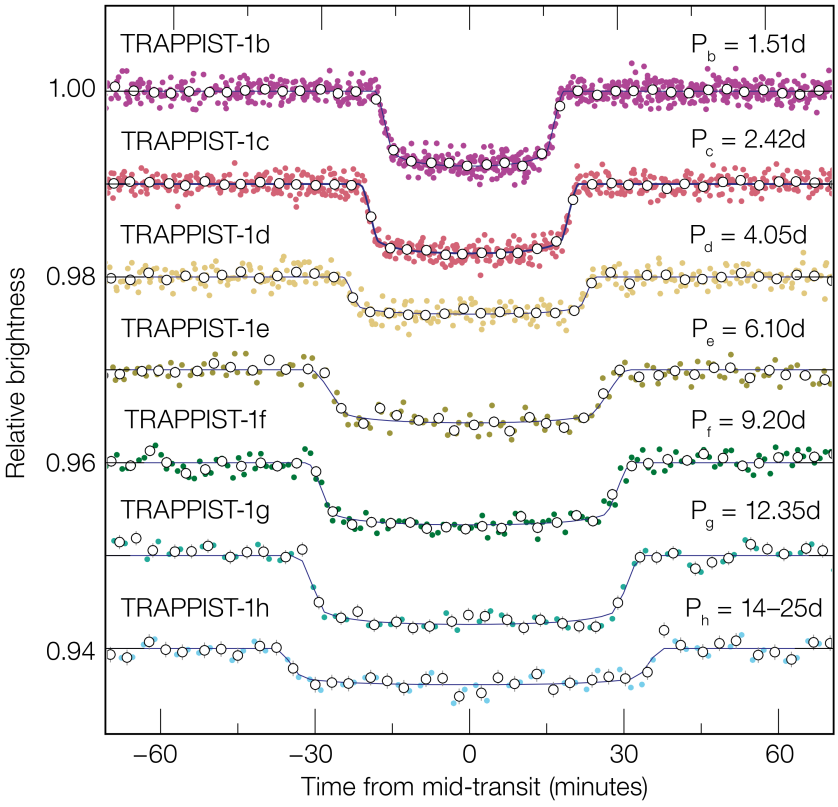

Figure 2.4: Dips in brightness observed in the star TRAPPIST-1 as its orbiting planets transit its disk. Larger planets create deeper dips and further planets create longer dips.

For a transit detection to be effective, the orbital plane of the investigated planet must be aligned with the observer's line of sight. This is the method employed by the Kepler

mission, which by 2024 has detected about 2778[2] exoplanets through this method alone.

The probability of the visibility of a transiting planet varies with the radius of the star and the planet and its orbital separation, a: [36]

$$Prob_{transit} = \frac{(R_{star} + R_{planet})}{a}. \tag{2.1}$$

Numerous ground-based transit surveys are currently engaged in the search for giant planets with short orbital periods. Achieving higher levels of photometric precision to detect smaller planets is challenging with ground-based methods due to atmospheric limitations. On the contrary, space-based observatories have the potential to detect even the subtle photometric transits of Earth-like planets orbiting solar-type stars at a distance of 1 astronomical unit. [36]

In some cases, this method is adopted in combination with the radial velocity method, thereby facilitating the acquisition of more precise measurements.

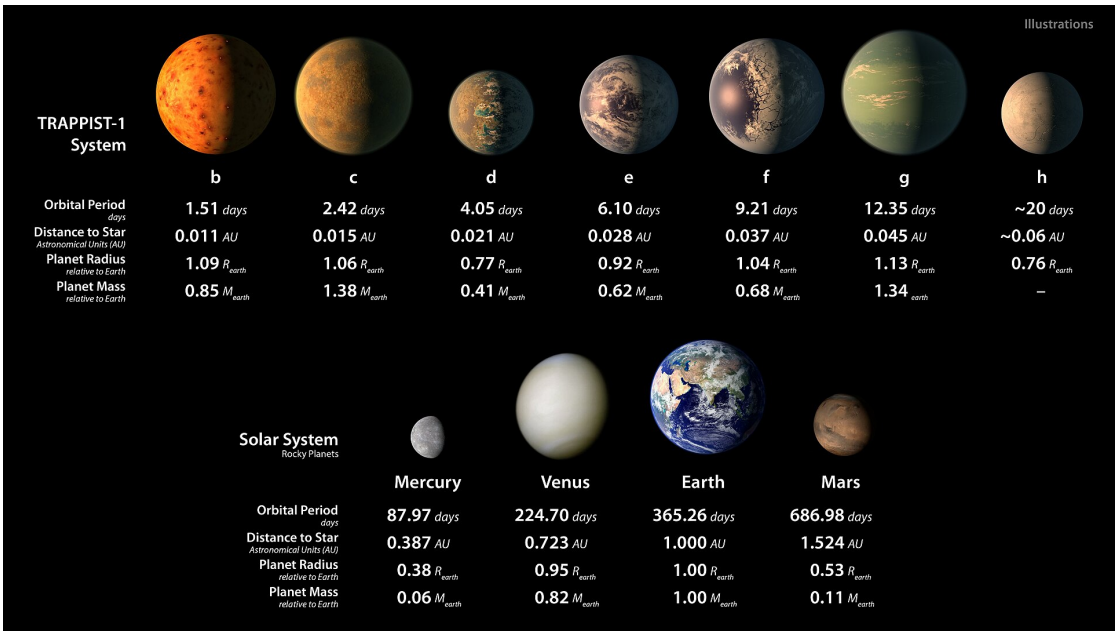

Figure 2.5: Artistic representation of the planetary system of the red dwarf TRAPPIST-1, discovered through the transit method, and comparison with the inner planets of the Solar System. The TRAPPIST-1 system is one of the main candidates for hosting life, as its planets e, f and g are potentially located within the habitable zone.[3]

Radial velocity or Doppler spectroscopy

This method makes use of variations in the radial velocity of the star with respect to the observer, detected by displacements in the star's spectral lines caused by the Doppler effect, induced by the revolution motion of both star and planet around their common centre of mass.[37] The spectral lines of a star exhibit a shift towards the blue end of the spectrum when moving closer to the observer, known as blueshift, and towards the red end when moving away, known as redshift[2] (see Figure 2.6 for reference).

This is the methodology which enabled the discovery of the first confirmed exoplanet, 51 Pegasi b, in 1995. As of 2024, about 1075 exoplanets have been detected by employing the radial velocity technique[2]. Since it is based on the gravitational interaction between two celestial bodies orbiting a shared centre of mass, the radial velocity method has also enabled the discovery of numerous binary stars.[36]

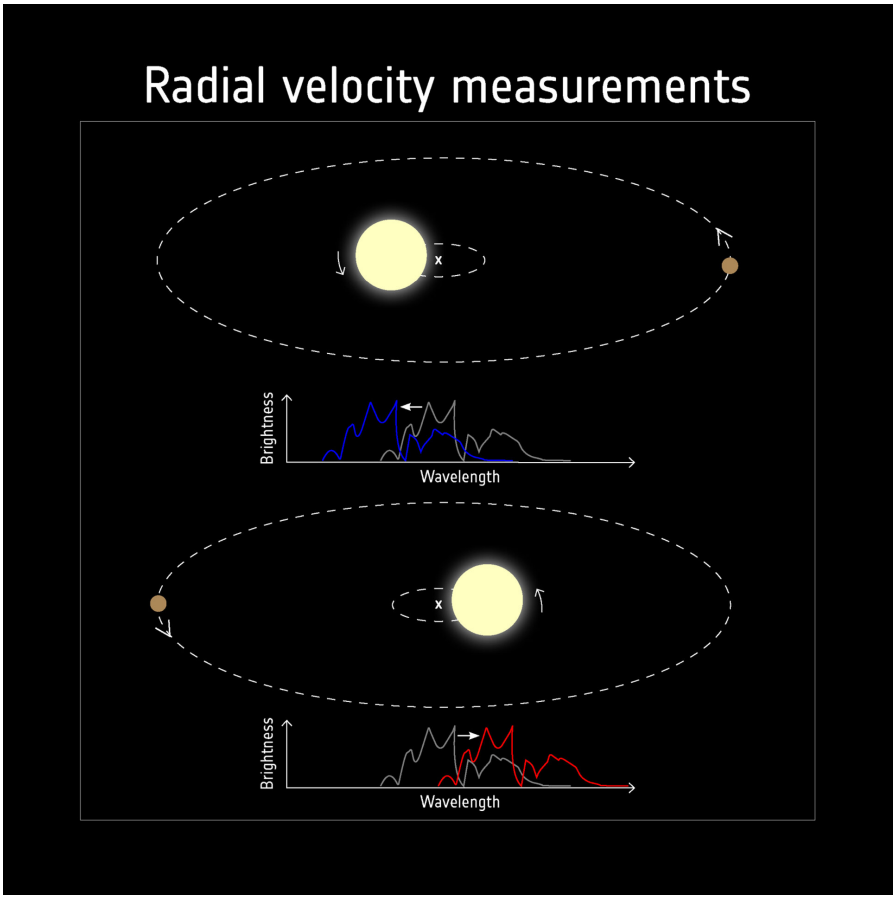

Figure 2.6: Blueshift and redshift caused by the "wobble" in the star motion caused by the gravitational pull of the planet.[4]

The latest technological developments have enabled the detection of radial velocity variations as small as 1 m/s.[38]

Gravitational microlensing

The gravitational field of a star acts as a sort of magnifying lens, intensifying the light of a distant background star (the "source"). When this magnification shows time-varying distortions or anomalies, this could imply the presence of a planet orbiting the studied star. The gravitational microlensing method is particularly sensitive to planets situated at a distance of about 1-10 AU from Sun-like stars.[39]

The magnification factor is influenced by the specific geometric conditions, with the highest level reached when the lens is positioned at the closest possible distance from the source. Depending on the properties of the radiation source and the lens, amplification occurs over various time spans, ranging from hours to years. A more intricate light curve may be observed from the distant source if the foreground lensing object is gravitationally complex, such as a star system with planets or a cluster of galaxies. This intricacy arises due to the time-varying magnification resulting from the evolving alignment geometry[2].

Direct imaging

Planets exhibit significantly low luminosity in comparison to their respective host stars. A Sun-like star emits light that is roughly a billion times more intense than the reflected light

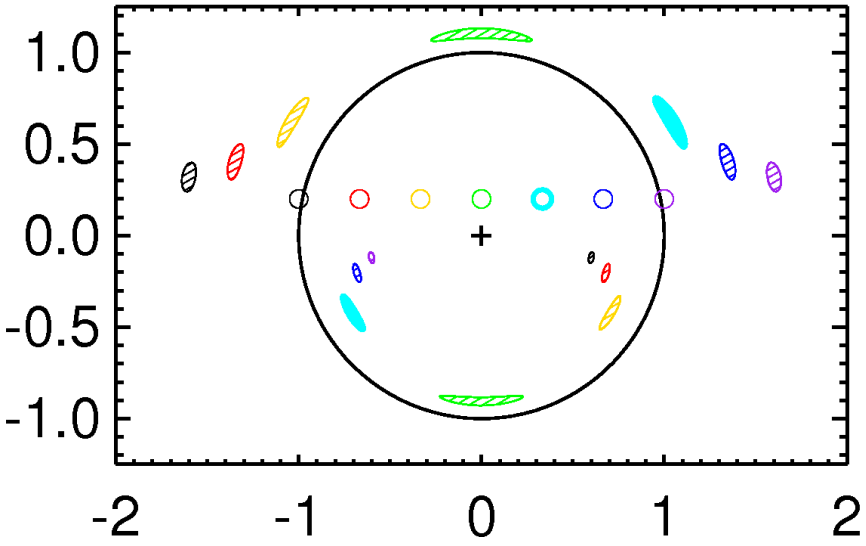

Figure 2.7: Images of a lensed source star. The location of the source is denoted by small circles, while the filled ovoids represent the lensed images corresponding to each source position. The Einstein ring is illustrated by the large black circle. The lens star is situated at the center, identified by the plus symbol. The Einstein ring is the area within which the source is lensed, if it is nearly aligned with the lens along the line of sight. Its angular size depends on the mass of the lens star and on the trigonometric parallax between the source and the lens.[5]

emanating from any exoplanet in its orbit. The task of detecting such feeble luminosity is challenging due to the overwhelming glare caused by the parent star. Therefore, it becomes crucial to obstruct the light originating from the star to diminish the glare, while allowing the planet's light to be discernible; achieving this goal presents a substantial technological hurdle that necessitates exceptional optothermal stability[40]. All exoplanets that have been directly observed are characterized by their substantial size (exceeding the mass of Jupiter) and considerable distance from their host stars.

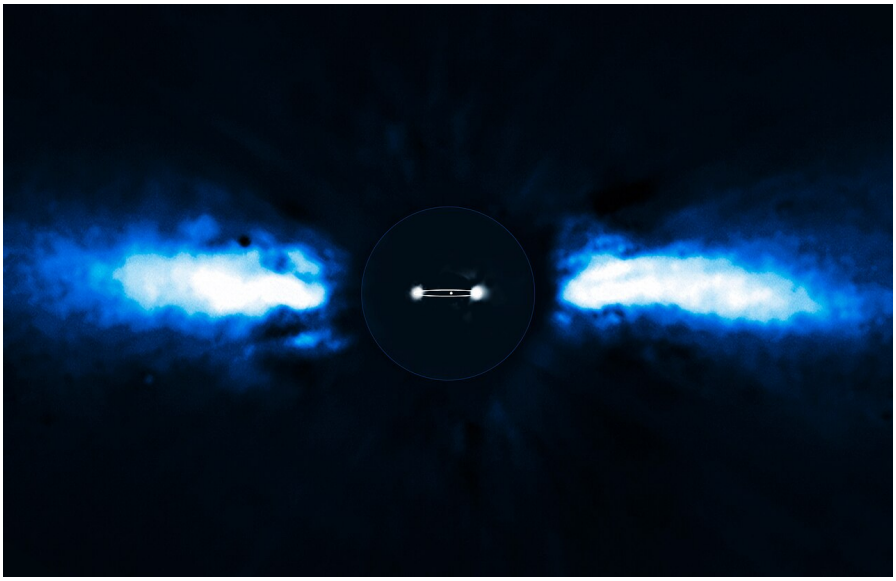

Figure 2.8: Direct image of planet Beta Pictoris b.[6]

2.2 Astrometry for exoplanet detection: state of the art and challenges

2.2.1 Fundamentals and main challenges of the technique

Astrometry is the discipline that deals with providing the most precise measurements possible of a star's position in order to accurately resolve its proper motion, its parallax displacement and its orbital motion resulting from gravitational interaction with other bodies in its system[5] (Figure 2.9). In the field of exoplanetary science, it is exploited to study the perturbations in the motion of the star under observation resulting from the gravitational influence of a potential planet orbiting with it: if a 'unseen companion' revolves together with its parent star around a common centre of mass, the latter's apparent motion - derived from the combination of its proper motion and heliocentric parallax displacement - will appear to be irregular (Figure 2.10).

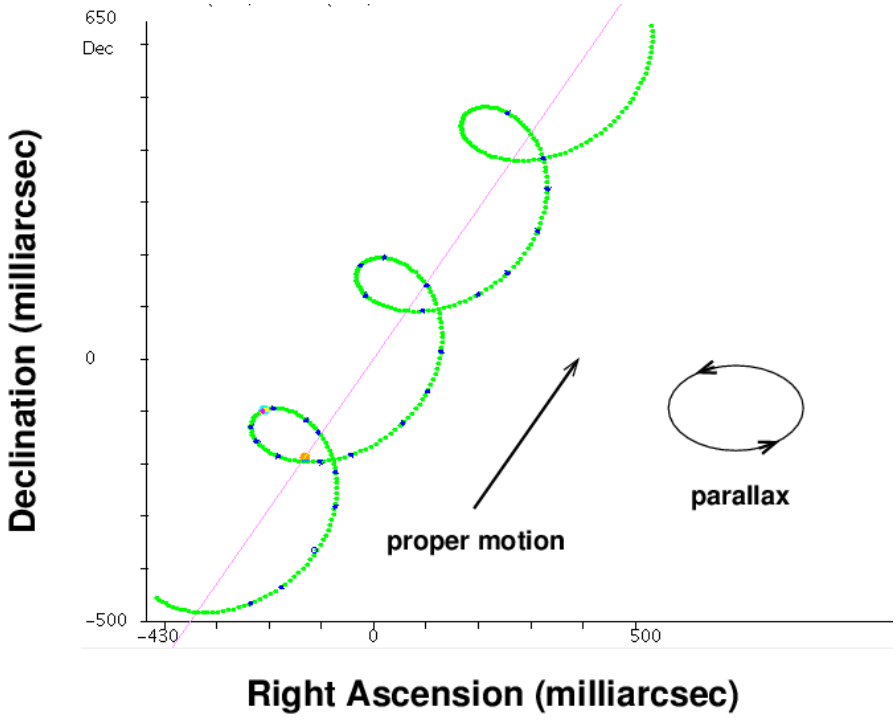

Figure 2.9: Combination of the proper angular motion of a star around the center of the Milky Way and the periodic parallax displacement observed as Earth orbits the Sun. The resulting apparent motion is shown as observed over a three-year timespan.[7]

The variation in the motion of the observed star is all the more appreciable the larger the orbit of its planet, and thus the longer its orbital period, increasing also the amplitude of the centre of mass displacement. For this reason, the orbital periods of planets observable through astrometry typically span several years.[5]

It is evident that although this method has clear advantages, such as the potential for providing an accurate estimate of the mass of the investigated planet and the possibility of carrying out this type of observation even for systems with orbital planes perpendicular to the observer's line of sight, it is also challenging to implement. This is because detecting the displacement of the star's centre of mass due to the gravitational influence of a planet requires an accuracy of an order ranging, depending on the size of the planet itself, from less than a milli-arcsecond (mas) for Jovian planets to less than a micro-arcsecond (μas) for Earth-like planets.

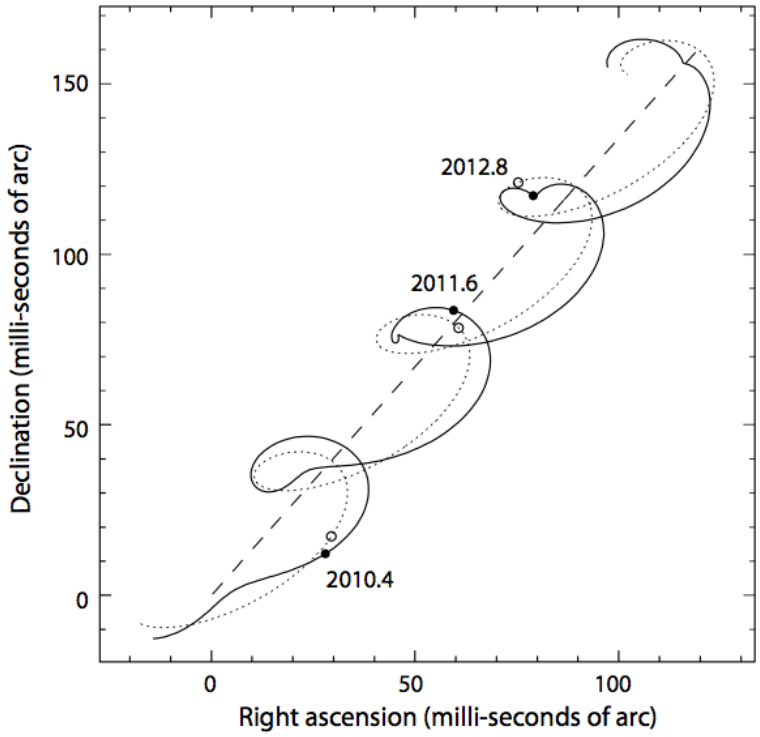

Figure 2.10: Perturbed observed trajectory of a star due to its revolution with the planet around their shared center of mass.[7]

Furthermore, the necessity to maintain highly precise measurements over extended periods calls for technologies that have historically proven challenging to develop. Nevertheless, this method has significant potential for not only the detection of exoplanets but also for confirming the presence of these planets, also providing better mass and orbital parameter estimates, when used in conjunction with other techniques.[5]

The precision σ of astrometric measurements is primarily constrained by the capacity to determine the position of the image of a point-like source on a detector. In the diffraction limit, this precision is linked to the wavelength λ, aperture size D, and signal-to-noise ratio S/N, which is commonly restricted by, at least, photon noise ($S/N \sim \sqrt{N_p}$):

$$\sigma \propto \frac{1}{S/N} \frac{\lambda}{D}. \tag{2.2}$$

Consequently, the attainable astrometric accuracy increases with the telescope aperture size. For ground-based observations, the primary source of error is the turbulence in the Earth's atmosphere above the telescope. This can be addressed by converting seeing-limited into nearly-diffraction-limited observations through adaptive optics, and by off-axis fringe tracking in dual-field interferometry. Instruments in space circumvent atmospheric disturbances entirely, enabling access to mostly diffraction-limited observations, making them well-suited for high-precision astrometry studies. [5]

In order to achieve a reliable solution and reduce the potential for correlations among proper, parallactic, and orbital motion, it is necessary to have a minimum timespan of one year and to ensure appropriate sampling of the orbital period.[5]

2.2.2 Ground based, space-borne, local and global astrometry

A basic technique entails the repetitive imaging of a specific target star and the measurement of its motion in relation to background reference sources. This methodology has been adopted by numerous medium to large ground-based telescopes, enabling the achievement of accuracies below 0.1 mas, which represents a level of performance necessary to effectively detect massive exoplanets.[5] Nevertheless, the employment of specific technologies, such as optical interferometers which enable to achieve a significant effective aperture size through the integration of light from several telescopes, can result in an attainable precision of 0.01 mas.[5] At the ESO Very Large Telescope (VLT) Interferometer, the GRAVITY interferometric instrument, a 4-way beam combiner in K band with astrometric capabilities, achieves at present an astrometric accuracy of the order of a few tens to a few hundreds of micro-arcoseconds.[41] It is anticipated that further improvements in precision will be made once ESO Extremely Large Telescope (ELT) becomes operational (around 2028). The telescope will be equipped with a primary mirror with a diameter of 39 metres, which is almost five times the diameter of the primary mirror of the VLT's Unit Telescope (8.2 metres).[41, 42]

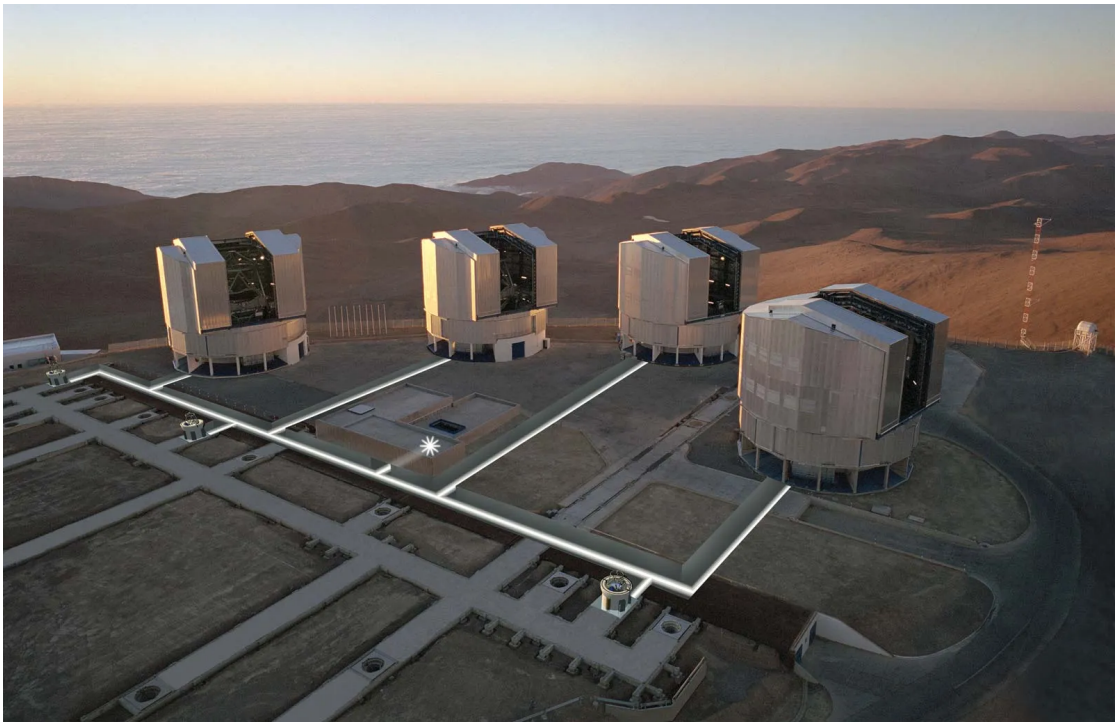

Figure 2.11: The four Unit Telescopes of ESO Very Large Telescope.[8]

It is evident that ground-based astrometry is inherently constrained to a local nature, given the fixed positioning of the telescope. However, observing only a limited portion of the celestial sphere typically by employing observatories with large apertures allows for greater accuracy than a global astrometric survey. The only three planets detected through the astrometric method have all been discovered through ground-based astrometry.[43]

On the other hand, space astrometry can also be global, enabling the comprehensive mapping of the Galaxy's stars and their positions through repeated scanning of the entire celestial vault, in order to construct a global and absolute reference frame. Notable examples of this approach include the Hipparcos mission and the more recent Gaia mission. While the Hipparcos data lacked the requisite precision to discern the astrometric orbits of known exoplanets, Gaia has been able to achieve a higher level of accuracy, with a

precision of less than 0.1 mas.[5, 44]

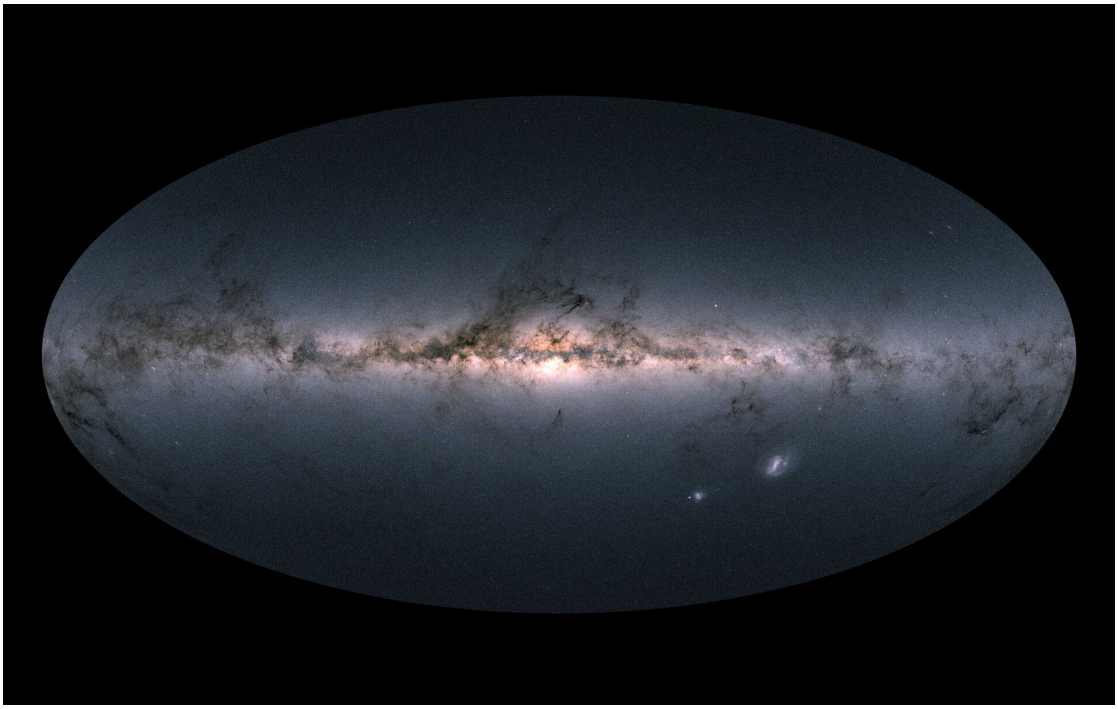

Figure 2.12: Gaia's all-sky view of the Milky Way Galaxy and neighbouring galaxies, based on measurements of nearly 1.7 billion stars.[9]

The future frontier of space astrometry will be the application of novel technologies to attain sub-micro-arcsecond accuracy, thus enabling the detection of Earth-like planets and the execution of more precise local surveys.

A number of potential missions have been proposed for this objective: two prominent examples are Theia, a mission designed to detect sub-micro arcsecond position variations of the ∼50 nearest Solar-type stars, with the aim of determining orbits and true masses of Earth twins in their habitable zones[20]; and TOLIMAN, a mission devoted to astrometric observation of the Alpha Centauri system in order to detect the presence of rocky planets orbiting the closest star system to our own.[45]

It is in this forward-looking and ambitious context that the RAFTER concept is proposed[11].

2.3 The RAFTER concept

2.3.1 Definition and rationale

The RAFTER (Ring Astrometric Field Telescope for Exoplanets and Relativity) optical instrument is designed with the aim of attaining high-quality imaging and particularly accurate astrometric performance across a relatively large field of view. The latter condition is achieved by ensuring that circular symmetry is maintained at every level of the optical system, all the way to the focal plane.[10]

The rationale for an annular field telescope is to optimize the telescope's performance over an annular region located at a certain radius from the optical axis. This allows the simultaneous observation of any pair of targets with a separation ranging from zero to its angular diameter. However, the annular field may not be convenient for some applications, such as performing a uniform scan of a large area.[11]

2.3.2 Optical design

The design of RAFTER is based on a traditional Three Mirror Anastigmat (TMA), but has been optimized to take full advantage of a complete ring within the corrected field. The TMA telescope concept is a design that uses three mirrors with special shapes to correct distortions and improve image quality over a large area.[11, 10] RAFTER uses a combination of three curved mirrors and a flat folding mirror to correct distortions and improve image quality.[11] The telescope configuration can be observed in Figure 2.13. An interesting feature is that the secondary (M2) and tertiary (M3) mirrors are nested within each other, as well as the pair constituted by the primary (M1) and the flat folding mirror (FM). The input pupil and all mirrors are annular, utilizing only a ring-shaped circular area. The flat FM serves a dual purpose of directing the optical path from M2 to M3 and from M3 to the focal plane (FP), which consists of a ring of CCD detectors encircling the main tube of the telescope. This setup is characterized by its high level of symmetry and compactness, measuring 1.7 m in length and 1.2 m in diameter.[10]

These characteristics contribute to the design's scalability, enabling a potential implementation as a payload for spacecrafts with limited envelope, such as CubeSats.[11]

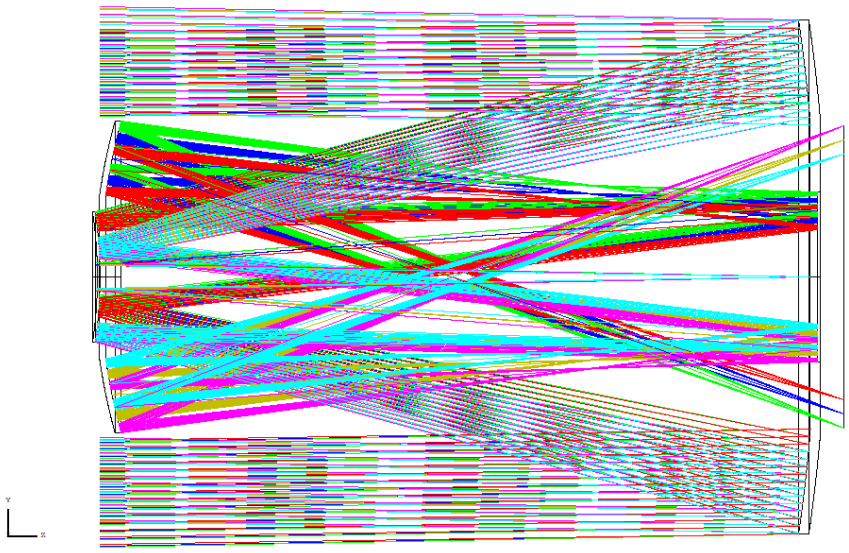

Figure 2.13: The configuration of the RAFTER telescope involves positioning the focal plane (FP) on a circular structure that encircles the input beam.[10]

2.3.3 Details of the observations

The RAFTER optical instrument features a field of view and associated detection system arranged in a circular strip centered on the optical axis projection. The optical system maintains circular symmetry, ensuring the instrument's response symmetry. The annular field of RAFTER (with radius θ and width $\delta\theta$) enables simultaneous observation of source pairs. Figure 2.15, where $\theta = 1^\circ$ and $\delta\theta = 0^\circ.1$, illustrate this concept: the target star T is positioned at the center, with four reference stars (R1, R2, R3, and R4) placed at extreme positions on both axes. By setting the optical axis of the telescope at suitable points on the dotted circle, the target and any object within the shaded area (dashed circle) can be observed simultaneously, effectively pivoting the field of view around the target.[10]

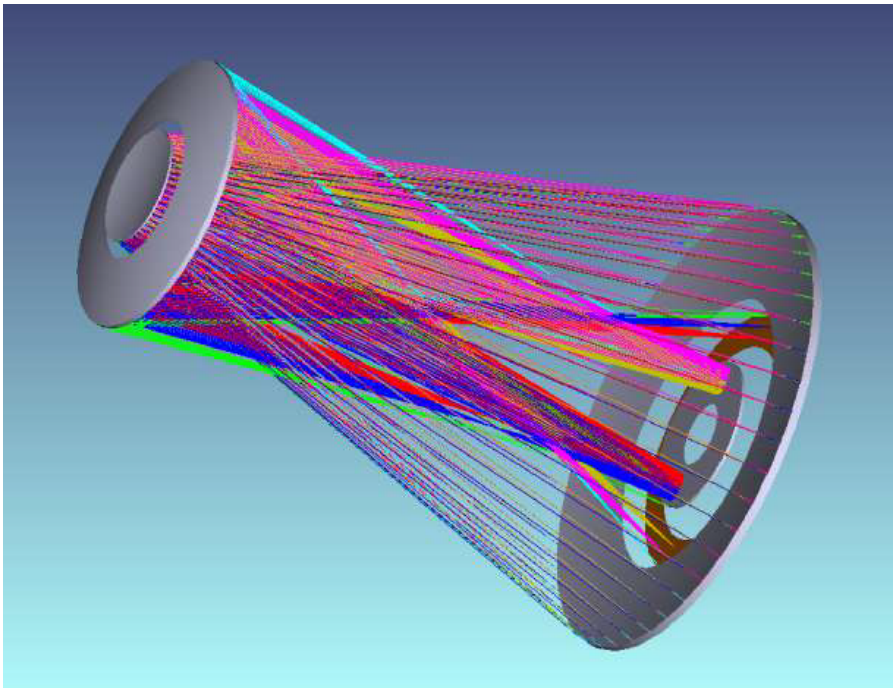

Figure 2.14: Telescope 3D view.[11]

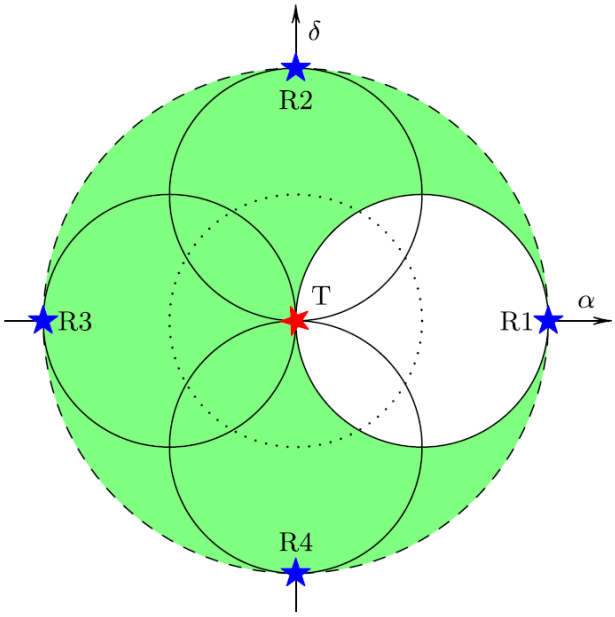

Figure 2.15: Field (2° radius, shaded) accessible to the target star T (center) by pointing the telescope along the dotted circle (1° radius): reference stars R1, R2, R3 and R4 are shown at ±2° on either coordinate.[10]

This approach allows flexibility in selecting the desired field of view around a specific target, based on performance optimization criteria. For instance, a region around the science target may be chosen, including the brightest accessible reference star; other criteria such as maximizing the number of field stars can also be considered. This framework proves to be effective for implementing precise narrow angle astrometry by utilizing available references (such as the Gaia catalog) and potentially enhancing it with

additional observations to refine individual source parameters.[10]

Chapter 3

Theoretical background

The goal of this Chapter is to briefly outline the theoretical concepts that are essential for comprehending the study carried out in this thesis, which will be detailed in subsequent Chapters. The first section will set out the fundamental principles of the kinematics and attitude dynamics of a rigid body, to which the spacecraft under examination will be approximated, which will be exploited to model the manoeuvres simulated in the present work. In the second part of the Chapter, an overview of some aspects of optimal control theory and trajectory optimization will be provided, focusing in particular on the direct methods used in this work.

3.1 Fundamentals of spacecraft attitude kinematics and dynamics

In order to describe the attitude of a rigid body and to determine its evolution as a function of its initial angular velocity and applied torques, it is necessary to detail the concepts of Euler angles and quaternions and introducing Euler's equations of motion.[46]

3.1.1 Euler angles

Definition and rotations

Euler angles are a set of three independent quantities that are used to describe the orientation of a rigid body in a three-dimensional space or, alternatively, to define the orientation of one reference frame with respect to another. The application of these angles enables the conversion of vector components from an initial reference frame $\mathcal{F}_1 = (X_1, Y_1, Z_1)$ with unit vectors $(\hat{i}, \hat{j}, \hat{k})$ into a second reference frame $\mathcal{F}_2 = (X_2, Y_2, Z_2)$ with init vectors $(\hat{l}, \hat{m}, \hat{n})$.[47]

Each Euler angle represents the quantity by which the initial system is rotated around a specific axis. Typically three rotations are required for the initial system to align with the target system. It should be noted that the order of these rotations is not commutative.[46] Indeed, there are multiple orders of rotation that can be employed to align two reference systems.

One of the most frequently exploited transformation sequences that most clearly exemplifies the operation of Euler angles is the **3-2-1** (or *Bryan angles*), which involves a first rotation of a ψ angle around the Z axis of the starting reference frame, a second rotation of a θ angle around the Y axis of the reference frame obtained from the previous rotation, and finally a final rotation of a ϕ angle around the X axis of the reference frame

derived so far, to finally reach the orientation of the target reference frame.[47, 46] The aforementioned transformation is illustrated in graphical form in Figure 3.1.

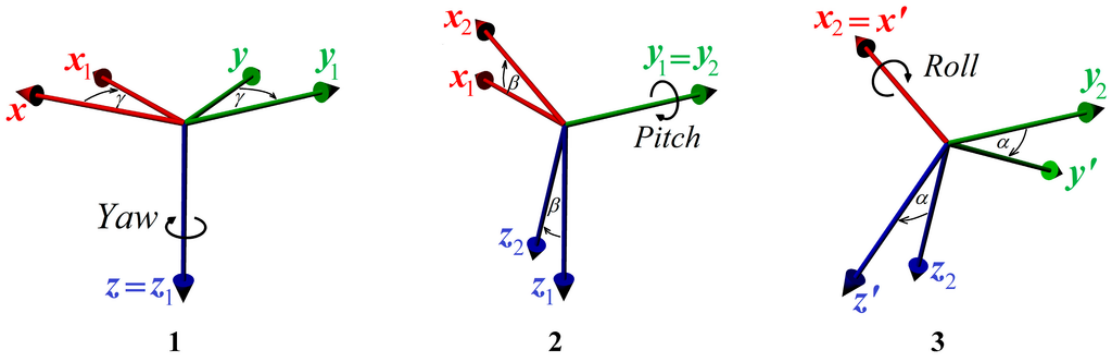

Figure 3.1: 3-2-1 or Bryan angles transformation. In this image, the angles ψ, θ, ϕ are designated as γ, β, and α, respectively.[12]

Each rotation represents a transformation from one reference frame to another, which can be expressed in matrix form. With regard to the 3-2-1 transformation, the following applies[47]:

$$\Psi = \begin{bmatrix} cos\psi & -sin\psi & 0 \\ sin\psi & cos\psi & 0 \\ 0 & 0 & 1 \end{bmatrix} \tag{3.1}$$

$$\Theta = \begin{bmatrix} cos\theta & 0 & sin\theta \\ 0 & 1 & 0 \\ -sin\theta & 0 & cos\theta \end{bmatrix} \tag{3.2}$$

$$\Phi = \begin{bmatrix} 1 & 0 & 0 \\ 0 & cos\phi & -sin\phi \\ 0 & sin\phi & cos\phi \end{bmatrix} \tag{3.3}$$

The transformation matrices Ψ, Θ and Φ are orthogonal, and thus their inverse is equal to their transpose. The final transformation matrix from the initial reference frame to the desired one will then be given by the product of the three transformation matrices[47]:

$$[L] = [\Psi][\Theta][\Phi]. \tag{3.4}$$

One of the most common employed transformations in the field of aerospace engineering is the **3-1-3** (or *proper Euler angles*) transformation[47].

Angular velocity and singularity

Considering the reference frame $\mathcal{F}_2$ with unit vectors $(\hat{l}, \hat{m}, \hat{n})$ mentioned at the beginning of this section as the initial reference frame, $\mathcal{F}_1$ with unit vectors $(\hat{i}, \hat{j}, \hat{k})$ as the target reference frame and a **3-2-1** rotation sequence, it is possible to explicate the the angular velocity of the initial reference frame, expressed in the coordinates of the target reference frame, as follows[47]:

$$\omega_r = \dot{\psi}\hat{n} + \dot{\theta}\hat{m}' + \dot{\phi}\hat{i} = \dot{\psi}_1\hat{k} + \dot{\theta}_1\hat{j} + \dot{\phi}\hat{i}, \tag{3.5}$$

with

$$\dot{\psi}_1 = \Psi^{-1}\Theta^{-1}\dot{\psi}_{2'} \tag{3.6}$$

and

$$\dot{\theta}_1 = \Psi^{-1}\dot{\theta}_{2''}. \tag{3.7}$$

Where subscripts $2'$ and $2''$ refer to the two intermediate reference frames $\mathcal{F}_{2'}$ and $\mathcal{F}_{2''}$ obtained through the first ψ rotation and the second θ rotation respectively. Rewriting the angular velocity by making its components explicit in matrix form yields[47]:

$$\omega_r = \begin{bmatrix} \omega_{x_1} \\ \omega_{y_1} \\ \omega_{z_1} \end{bmatrix} = \begin{bmatrix} 1 & 0 & -sin\theta \\ 0 & cos\phi & sin\phi cos\theta \\ 0 & -sin\phi & cos\phi cos\theta \end{bmatrix} \begin{bmatrix} \dot{\phi} \\ \dot{\theta} \\ \dot{\psi} \end{bmatrix}. \tag{3.8}$$

Inverting Expression 3.8 results in the **equations of kinematics with Euler angles**, i.e. their variations over time, for a **3-2-1 rotation sequence**. In matrix form, these equations are expressed as follows[47]:

$$\begin{bmatrix} \dot{\phi} \\ \dot{\theta} \\ \dot{\psi} \end{bmatrix} = \frac{1}{cos\theta} \begin{bmatrix} cos\theta & sin\phi sin\theta & cos\theta sin\theta \\ 0 & cos\phi cos\theta & -sin\phi cos\theta \\ 0 & sin\phi & cos\phi \end{bmatrix} \begin{bmatrix} \omega_{x_1} \\ \omega_{y_1} \\ \omega_{z_1} \end{bmatrix} \tag{3.9}$$

. From this expression, the principal issue in using Euler angles becomes clear: the presence of the cosine of θ in the denominator leads to a singularity if the value of θ is $\frac{\pi}{2}$ or $\frac{3}{2}\pi$, making it impossible to uniquely distinguish all angles.[47] Because of this limitation, certain configurations of Euler angles can result in multiple representations of the same orientation, causing ambiguity in describing the exact position of an object in space.[46]

In the case of a **3-1-3 rotation sequence** the kinematics equations with Euler angles in matrix form become[47]:

$$\begin{bmatrix} \dot{\phi} \\ \dot{\theta} \\ \dot{\psi} \end{bmatrix} = \frac{1}{sin\theta} \begin{bmatrix} sin\psi & cos\psi & 0 \\ sin\theta cos\psi & -sin\theta sin\psi & 0 \\ -cos\theta sin\psi & -cos\theta cos\psi & sin\theta \end{bmatrix} \begin{bmatrix} \omega_{x_1} \\ \omega_{y_1} \\ \omega_{z_1} \end{bmatrix}. \tag{3.10}$$

The singularity in this case is found for $\theta = 0, \pi$ due to the presence of the sine of θ in the denominator[47].

The singularity is identified for any rotation with Euler angles, occurring at $\frac{\pi}{2}$ and $\frac{3}{2}\pi$ for asymmetrical rotation sequences and at 0 and π for symmetrical rotation sequences.[47] The presence of this singularity represents the primary disadvantage of Euler angles. While they are simple to represent in three-dimensional space and intuitive to interpret, they are challenging to compute and can often result in ambiguity when describing a specific orientation.[46]

3.1.2 Quaternions

Quaternions, also known as Euler parameters, are a mathematical extension of complex numbers used to represent orientations and rotations in three-dimensional space.[46] They are often employed for this purpose in place of Euler angles, as they essentially allow computationally complex trigonometric expressions to be transformed into simpler to implement algebraic expressions, while also making it possible to circumvent the disadvantageous singularity inherent in Euler angles. This discussion will not dwell on the mathematical intricacies of quaternions; instead, it will provide a concise illustration of the concept and emphasise the practical implications of its utilization.

To introduce these quantities, it is first essential to state **Euler's eigenaxis rotation theorem**, which asserts the feasibility of rotating a fixed frame $\mathcal{F}_1$ to align with any

arbitrary frame $\mathcal{F}_2$ by executing a straightforward rotation about an axis a that remains fixed in both frames. This axis, known as **Euler's rotation axis** or **eigenaxis**, exhibits identical direction cosines within the two frames under consideration.[46]

The Euler axis is defined in such a way that[47]:

$$\sqrt{a_1^2 + a_2^2 + a_3^2} = 1. \tag{3.11}$$

Its components are identical in both reference frames[47]:

$$\hat{a} = a_{x_1}\hat{i} + a_{y_1}\hat{j} + a_{z_1}\hat{z} = a_{x_2}\hat{l} + a_{y_2}\hat{m} + a_{z_2}\hat{n}. \tag{3.12}$$

A quaternion is defined uniquely in terms of the Euler axis a and the angle of rotation α around said axis. A rotation of the vector $\vec{v}$ by an α angle about the Euler axis, from frame $\mathcal{F}_1$ to $\mathcal{F}_2$, results in[47]:

$$\vec{v_{rot}} = \vec{v_{//rot}} + \vec{v_{\perp rot}} = \vec{v_{//}} + \vec{v_{\perp rot}}. \tag{3.13}$$

The parallel component of $\vec{v}$ is conserved both before and after rotation in accordance with the principles set forth by Euler's eigenaxis rotation theorem. The perpendicular component will instead be[47]

$$\vec{v_{\perp rot}} = \vec{v_{\perp}} cos\alpha + (\vec{a} \times \vec{v_{\perp}}) sin\alpha. \tag{3.14}$$

The quaternion vector is constituted of four quantities, one scalar and three vectors, defined as follows given the Euler axis a and the angle of rotation α[46, 47]:

$$\begin{cases} q_0 = cos(\frac{\alpha}{2}) & \text{(scalar)} \\ q_1 = a_1 sin(\frac{\alpha}{2}) & \text{(vector)} \\ q_2 = a_2 sin(\frac{\alpha}{2}) & \text{(vector)} \\ q_3 = a_3 sin(\frac{\alpha}{2}) & \text{(vector)} \end{cases}$$

The attitude of a rigid body, such as the spacecraft here under study, can be expressed in quaternion form as $q = [q_0, q_1, q_2, q_3]^T$.

Kinematics equations with quaternions

The following Equation represents the kinematics of a rigid body expressed with quaternions[46, 17] (the demonstration of its derivation is omitted):

$$\dot{q} = \frac{1}{2} Q\vec{\omega} = \frac{1}{2}\vec{q}\Omega; \tag{3.15}$$

where

$$Q = \begin{bmatrix} -q_1 & -q_2 & -q_3 \\ q_0 & -q_3 & q_2 \\ q_3 & q_0 & -q_1 \\ -q_2 & q_1 & q_0 \end{bmatrix}$$

and

$$\Omega = \begin{bmatrix} 0 & -\omega_1 & -\omega_2 & -\omega_3 \\ \omega_1 & 0 & \omega_3 & -\omega_2 \\ \omega_2 & -\omega_3 & 0 & \omega_1 \\ \omega_3 & \omega_2 & -\omega_1 & 0 \end{bmatrix};$$

Explaining the scalar and vector part of the quaternion gives[46]:

$$\dot{q}_0 = -\frac{1}{2}\vec{\omega}\vec{q_v}; \tag{3.16}$$

$$\dot{q}_v = \frac{1}{2}(q_0\vec{\omega} - \vec{\omega} \times \vec{q_v}). \tag{3.17}$$

3.1.3 Euler's equation of motion

Euler's equation of motion is an important expression in rigid body dynamics that states the relationship between the time derivative of angular momentum and the total external torque applied to a body. It is employed to describe the rotational dynamics of a rigid body when subjected to the application of external moments.[46]

It is formulated from the **second fundamental law of rigid body dynamics**, which states that the time derivative of the angular momentum of a rigid body is equivalent to the overall external torque exerted on body B.[46] In vector form:

$$\frac{d\vec{h}}{dt} = \vec{M}; \tag{3.18}$$

Expressing the vector quantities in body coordinates results in:

$$\dot{h}_B + \vec{\omega}_B \times \vec{h}_B = \vec{M}_B; \tag{3.19}$$

The expression above, if the inertia tensor (a symmetric matrix which captures the moments of inertia of a body with respect to different axes, providing information about how mass is distributed and how the body resists rotational motion[46]) is constant, can be rewritten as:

$$I\dot{\omega}_B + \vec{\omega_B} \times I\vec{\omega_B} = \vec{M}_B, \tag{3.20}$$

bearing in mind that $\vec{h_B} = I\vec{\omega}$ if the origin of the rotating body reference frame is in the centre of mass of the rigid body, which rotates solely around said point.

When the body axes are also principal inertia axes, the inertia tensor becomes diagonal and the Euler's equation of motion for a rigid body are thus derived:[46]

$$\begin{cases} I\dot{\omega}_x + \omega_y\omega_z(I_z - I_y) = M_x \\ I\dot{\omega}_y + \omega_x\omega_z(I_x - I_z) = M_y \\ I\dot{\omega}_z + \omega_y\omega_x(I_y - I_x) = M_z \end{cases} \tag{3.21}$$

The equations above can be integrated as a function of the applied torque, yielding the variation with time of the angular velocity components, which, in turn, can be used to assess the temporal evolution of the Euler's angles (or quanternions), thus defining how the rigid body attitude changes over time.[46]

3.2 Notions of optimal control theory

The majority of the following discussion is derived from Kelly's paper "*An introduction to trajectory optimization: how to do your own direct collocation*"[13] (2017), which has been employed extensively as an exemplar to advance the work on which this thesis is based.

3.2.1 The trajectory optimization problem

For the sake of clarity, a *trajectory* can be defined as the path a system follows to transition from one state to another. The typical trajectory planning process involves determining the state variables (such as position and velocity) and control inputs (such as thrust) as they vary over time. *Trajectory optimization* is the collective term for a range of methods employed to identify the optimal trajectory by defining the the inputs to the system, namely the *controls* as functions of time.[13]

To illustrate the concept as clearly as possible, a simple example is given: how to move a block between two points, starting and finishing at rest, in a fixed amount of time.

The first step is to explicate the dynamics of the system, which describe its motion. In this case, the block is modelled as a point-mass that travels in one dimension, and the control input to the system consists of the force applied to the block. Using x to refer to position, v for velocity and u for control, i.e. the input force, the dynamics of the system can be written as[13]:

$$\dot{x} = v; \tag{3.22}$$

$$\dot{v} = u. \tag{3.23}$$

The objective is to move the block one unit of distance in one unit of time, ensuring that the system is stationary at both the beginning and end of the process. These constraints, displayed in Figure 3.2, are known as **boundary constraints** or **boundary conditions**[13]:

$$x(0) = 0; \tag{3.24}$$

$$x(1) = 1; \tag{3.25}$$

$$v(0) = 0; \tag{3.26}$$

$$v(1) = 0. \tag{3.27}$$

Figure 3.2: Boundary conditions for the block-move problem.

A solution to a trajectory optimization problem is *feasible* if it adheres to all constraints associated with the problem. In the example at hand, the only types of constraints present are those dictated by the dynamics of the system and the boundary constraints. However, in a general problem, there are commonly other types of constraints[13].

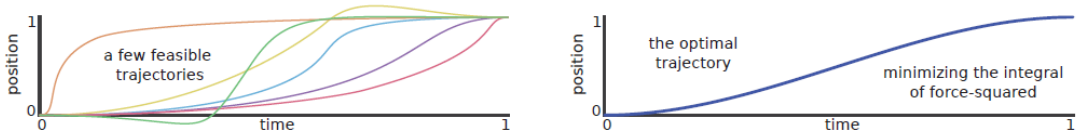

Figure 3.3: Feasible (left) vs optimal (right) trajectories.

Admissible controls refer to the collection of controls that generate feasible trajectories. Trajectory optimization focuses on determining the *optimal* trajectory among the feasible options, illustrated in Figure 3.3 and defined as the trajectory that best meets the *objective function*'s criteria for optimality.[13] Two common objective functions, which will be employed in the solution of the problem presented in this thesis (see Chapter 4), are the minimum integral of the square of the control and the minimum integral of the absolute value of the control:

$$min : J = \int_{t_0}^{t_f} u^2(t)\, dt \tag{3.28}$$

$$min : J = \int_{t_0}^{t_f} |u(t)|\, dt \tag{3.29}$$

There exist numerous methodologies for formulating trajectory optimization problems. This study will concentrate primarily on single-phase continuous-time trajectory

optimization problems, where the system dynamics remain continuous along the entire trajectory. Typically, an objective function consists of two term: a *boundary objective* denoted as $J(\cdot)$ and a *path integral* spanning the entire trajectory, with the integrand represented by $w(\cdot)$. A problem incorporating both components is referred to as being in *Bolza* form. Conversely, a problem featuring solely the integral term is classified as being in *Lagrange* form, while a problem with only a boundary term is categorized as being in *Mayer* form.[13] The examples presented in this work are all expressed in Lagrange form. In the Equation below, the first term is called the Meyer term, while the second is the Lagrange term.[13]

$$min : J(t_0, t_f, x(t_0), x(t_f)) + w(\tau, x(\tau), u(\tau)\, d\tau \tag{3.30}$$

Within the realm of optimization, the term *decision variable* is adopted to designate the variables that the optimization solver adjusts to minimize the objective function. Said decision variables are typically the initial and final time (t_0, t_f), in addition to the state and control trajectories, $x(t)$ and $u(t)$, respectively. The optimization process is governed by a range of constraints and requirements. Foremost among these constraints is the **system dynamics**, typically nonlinear in nature, which describes the temporal evolution of the system.[13]

$$\dot{x}(t) = f(t, x(t), u(t)) \tag{3.31}$$

The **path constraint** imposes restrictions along the trajectory.[13] For example, to use an illustration akin to the work of this thesis, a path constraint could be implemented to prevent the spacecraft's optical axis from pointing in the direction of the Sun during attitude manoeuvres.

$$h(t, x(t), u(t)) \leq 0 \tag{3.32}$$

The non-linear **boundary constraint** enforces restrictions on the initial and final states of the system.[13] In the present study, a boundary constraint could be employed to impose the initial attitude at which the spacecraft begins its manoeuvre and the final attitude it is required to have reached at the end of the manoeuvre.

$$g(t_0, t_f, x(t_0), x(t_f)) \leq 0 \tag{3.33}$$

Frequently, constant **path bounds** are imposed on the state or control variables.[13] For instance, one could impose a maximum allowable value of control torque that can be exertend on the spacecraft, or a maximum attainable angular velocity.

$$x_{low} \leq x(t) \leq x_{upp} \tag{3.34}$$

$$u_{low} \leq u(t) \leq u_{upp} \tag{3.35}$$

Lastly, it is often crucial to specify particular limits on the initial and final time and state. These limitations might be necessary to ensure that a solution to a path planning problem reaches the goal within a specified time frame or attains a specific target region within the state space.[13]

$$t_{low} \leq t_0 < t_f \leq t_{upp} \tag{3.36}$$

$$x_{0,low} \leq x(t_0) \leq u_{0,upp} \tag{3.37}$$

$$x_{f,low} \leq x(t_f) \leq x_{f,upp} \tag{3.38}$$

3.2.2 Direct methods

Most methods utilized in solving trajectory optimization problems can be categorized as either *direct* or *indirect*. A defining characteristic of direct approaches is the process of discretizing the trajectory optimization problem itself, often transforming the original problem into a **nonlinear program**. This transformation is referred to as **transcription**. Direct transcription methods generally achieve discretization of a continuous trajectory optimization problem through the approximation of all continuous functions within the problem statement as polynomial splines. A spline is essentially a function composed of a series of polynomial segments. The rationale behind using polynomials lies in their two crucial properties: they can be described by a limited (finite) number of coefficients, and their integrals and derivatives can be easily computed based on these coefficients.[13]

A nonlinear program refers to a specific type of constrained parameter optimization problem with nonlinear terms present in either its objective function or constraint function. A common formulation for a nonlinear program is outlined below[13]:

$$min : J(z)$$

$$subject\ to$$

$$f(z) = 0,$$

$$g(z) \leq 0,$$

$$z_{low} \leq z \leq z_{upp}$$

In certain instances, the utilization of a direct collocation method may result in the development of a linear or quadratic program rather than a non-linear program. This situation emerges when the constraints, which encompass system dynamics, manifest linearity, and the objective function is of a linear (resulting in a linear program) or quadratic nature (resulting in a quadratic program).[13]

This thesis employs a number of direct optimization methods. The most commonly utilized methods in this study are trapezoidal collocation and Hermite-Simpson collocation; however, there exist other available techniques, such as **orthogonal collocation** and **multiple shooting methods**[13, 48].

Trapezoidal direct collocation

Trapezoidal direct collocation operates under the assumption that an optimal trajectory could be approximated through a low-order spline. In this scenario, the dynamics, objective function, and control trajectories are represented by a linear spline, while the state trajectory is depicted by a quadratic spline, which is derived from the integration of the linear dynamics spline.[48] To compute the integration of a linear spline, the trapezoid rule is employed:[13]

$$\int_{t_0}^{t_F} w(\tau, \boldsymbol{x}(\tau), \boldsymbol{u}(\tau)) d\tau \approx \sum_{k=0}^{N-1} \frac{1}{2} h_k \cdot (w_k + w_{k+1}) \,. \tag{3.39}$$

Hermite-Simpson direct collocation

The Hermite-Simpson direct collocation method operates under the assumption that the optimal trajectory can be approximated through a spline of medium-order. This approach involves approximating the dynamics, objective function, and control trajectories with

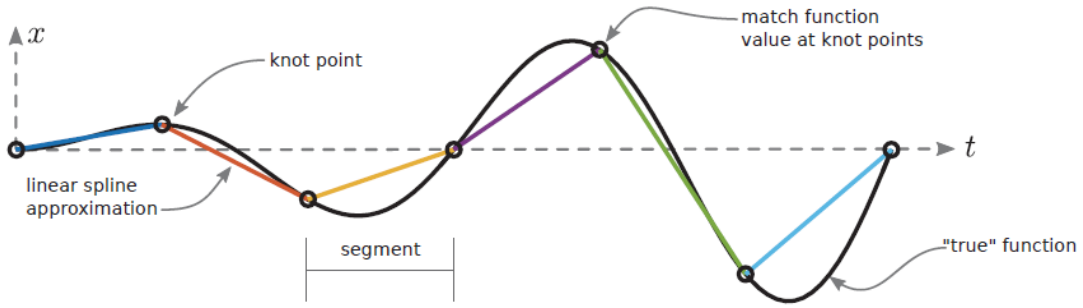

Figure 3.4: Function approximation using a linear spline.[13]

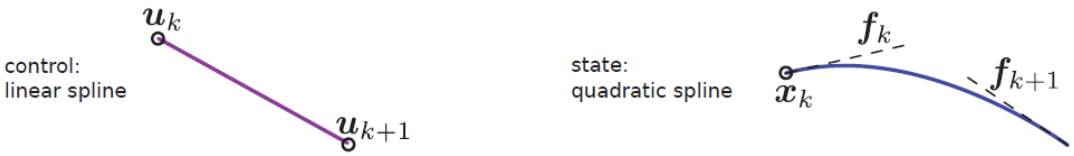

Figure 3.5: Linear and quadratic spline segments adopted to approximate the control and state trajectories for trapezoidal collocation.[13]

a quadratic spline, while the state trajectory is modeled using a cubic Hermite spline derived from the integration of the quadratic dynamics spline.[48] The integration of a quadratic spline is accomplished through Simpson's rule[13]:

$$\int_{t_0}^{t_F} w(\tau)d\tau \approx \sum_{k=0}^{N-1} \frac{h_k}{6}\left(w_k + 4w_{k+\frac{1}{2}} + w_{k+1}\right) \tag{3.40}$$

Two variations of this method exist: separated and compressed. In the separated version, the state at the midpoint of each trajectory segment is treated as a decision variable, and the Hermite interpolation is enforced through a constraint. On the other hand, in the compressed version, the state at the midpoint is determined based on the definition of the Hermite interpolant during the optimization process.[13]

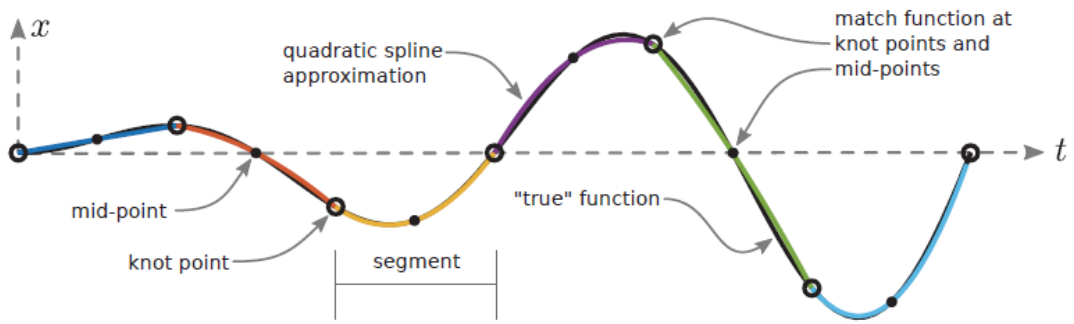

Figure 3.6: Function approximation using a quadratic spline. For the same number of segments, this approximation is more accurate than linear spline.[13]

Figure 3.7: Quadratic and cubic spline segments adopted to approximate the control and state trajectories for Hermite–Simpson collocation.[13]

Other direct methods

Chebyshev-Lobatto orthogonal collocation is based on expressing the complete trajectory through the utilization of a high-order Chebyshev orthogonal polynomial. The approach employed in this context could also be referred to as pseudospectral or global collocation, given that the entire trajectory is depicted using a singular segment as opposed to multiple segments. Orthogonal collocation techniques are commonly categorized into three groups: Gauss, Radau, and Lobatto. Within the Gauss method, neither endpoint of a segment serves as a collocation point; in the Radau method, one endpoint of the segment functions as a collocation point; and in the Lobatto method, both endpoints are designated as collocation points.[13]

The process of a **multiple shooting method** involves dividing the trajectory into segments and approximating each segment through an explicit simulation. Specifically, a **4th order Runge-Kutta method** is on occasion utilized for the study carried out in this thesis. To guarantee proper alignment between the end of each trajectory segment and the next one, a defect constraint is implemented. The interpolation of the solution trajectory, encompassing both control and state, is achieved through the approximation of a cubic Hermite spline. [13]

3.2.3 Indirect methods

Indirect methods involve the analytical construction of the necessary and sufficient optimality conditions, followed by their discretization and numerical solution. A key distinction between direct and indirect methods is that direct methods discretize before optimizing, while indirect methods optimize prior to discretizing. To illustrate the workings of an indirect method, let's consider a simple scalar optimization problem: minimizing $y = f(t)$. Fundamental calculus dictates that the minimum value $y^* = f(t^*)$ is attained when the derivative is zero, $y'(t^*) = 0$. It is also essential to verify that the curvature is positive, $y''(t^*) > 0$, to ascertain a local minimum rather than a local maximum (or saddle point). If both conditions are met, then $y^* = f(t^*)$ represents a local minimum. Though following a similar principle, an indirect optimization is more intricate in terms of constructing and solving the conditions. Conversely, a direct method minimizes $y(t)$ by generating a sequence of guesses where each subsequent guess improves upon the previous one: $y(t_0) > y(t_1) > ... > y(t^*)$.[13]

The primary advantage of an indirect method, in comparison to a direct method, lies in its generally higher accuracy and more dependable error estimation, stemming from the analytic formulations of the necessary and sufficient conditions developed during the formulation of the indirect problem.[13]

Numerous challenges are associated with indirect methods when contrasted with direct methods. Notably, the convergence region tends to be narrower for indirect methods compared to direct methods, necessitating a more precise initialization for an indirect

method. Additionally, the initialization process for an indirect method is complicated by the requirement to initialize the adjoint variables, which are not utilized in a direct method. Lastly, achieving an accurate solution with an indirect method typically demands the analytical construction of the necessary and sufficient conditions, a task that can be quite demanding.[13]

Chapter 4

Mission requirements and mathematical model

This Chapter first illustrates the physical properties of the hypothetical spacecraft bus evaluated to host the RAFTER optical instrument and the mission specifications and operations that it shall perform. In the second part, the mathematical model taking into account the dynamic system comprising the spacecraft in its environment and the manoeuvres studied is described in detail.

4.1 Overview of the RAFTER mission

4.1.1 Possible spacecraft bus configurations

In the present thesis, two possible configurations of the spacecraft intended to fulfil the RAFTER mission are presented: the first is the one originally conceived for the future use of the optical instrument, which consists of a 1 m diameter telescope on board a medium-class spacecraft with an envelope similar to those of the Kepler and Euclid observatories; the second involves a miniaturization of RAFTER and consequently of the entire spacecraft, this time in the form of an 18U CubeSat. The table below lists the inertial properties of each configuration.

	x-axis [m]	**y-axis [m]**	**z-axis [m]**	**Mass [kg]**
Nominal	1.5 (base diameter)	1.5 (base diameter)	2	1000
CubeSat	0.3	0.2	0.3	30

Table 4.1: Dimensions and mass of the spacecraft serving RAFTER for the nominal and CubeSat cases.

The envelope of the solar arrays is negligible, as they are body mounted in both cases. RAFTER has been envisaged as the only payload on board both spacecraft configurations.

4.1.2 Mission specifications

The main function of RAFTER is to point at specific portions of the celestial sphere and perform observations with high stability, so that the angular distance between the studied star and the reference star can be accurately measured. For this reason, it is therefore more logical to imagine that the spacecraft carrying RAFTER on board would simply

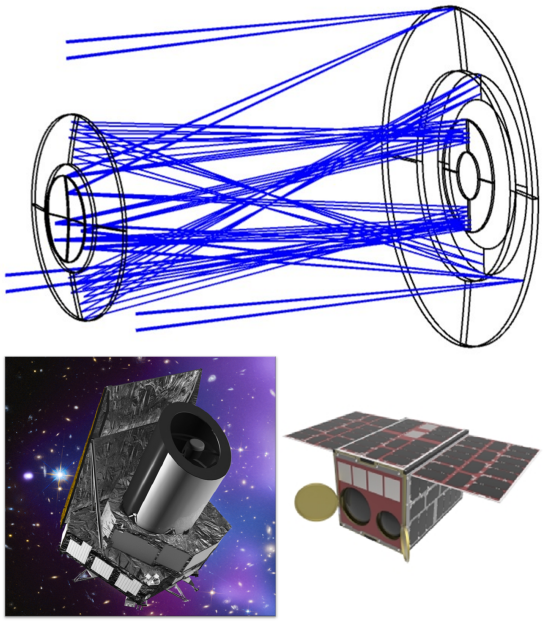

Figure 4.1: Optical drawing of the RAFTER instrument (top) and the two possible spacecraft configurations to house it on board: a medium-class space observatory with a comparable envelope to Euclid[14] or Kepler (bottom left) and a CubeSat[15] (bottom right).

observe specific targets for extended periods of time, instead of scanning larger portions of the celestial sphere by devoting less time to observations of each individual source[10].

The selected operational orbit is a halo or Lissajous orbit around the L2 Lagrange point of the Sun-Earth binary system, a location widely exploited in recent times by other space observatories such as Gaia, JWST and Euclid. The rationale for this choice lies in the possibility of maintaining the brightest celestial bodies, such as the Earth and the Sun, always facing the rear of the satellite, thus preventing them from entering the field of view of the optical instrument. Furthermore, this configuration enhances the thermal stability of the payload[10].

It is beyond the purpose of this thesis to provide a comprehensive account of the entire mission to be accomplished by RAFTER. Instead, an outline of the five phases into which it is imagined it is going to be divided is provided here:

- an initial **launch** phase;
- a subsequent **transfer and insertion phase** to the target orbit around the second Sun-Earth Lagrange point, L2, with a duration of approximately 30 days;
- a **commissioning phase**, for both the instrument and the spacecraft bus, beginning during the transfer phase and lasting about 3-6 months;
- the **operational phase**, the longest of the mission, which has been estimated to last 3 or 5 years;
- the **decommissioning phase** at the end of the operational life of the spacecraft.

An example of the transfer phase to the operational orbit is shown in Figure 4.2. The RAFTER satellite will perform its observations during the operational phase; they will be conducted on specific celestial portions through a '*step-and-stare*' criterion similar to that

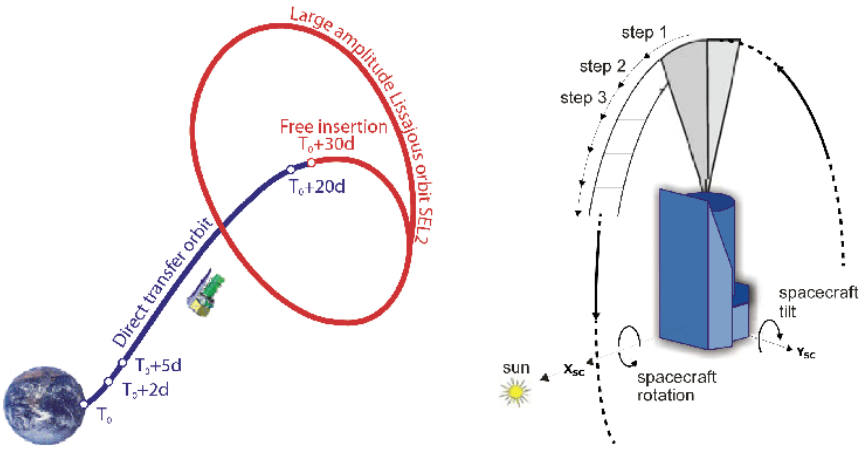

Figure 4.2: Example of a possible trajectory to be followed by the RAFTER spacecraft to reach its operational orbit around the L2 point of the Sun-Earth system and depiction of a typical observation manoeuvre[16]. In the case study of this thesis, the x-axis of the spacecraft-based reference frame has the opposite direction with respect to the picture.

of the Euclid mission. [16] In detail, each target will be observed for 20 minutes; then, a manoeuvre with a 20-minute duration moves the field of view to the next observation direction. The objective of this study is to model and simulate the aforementioned manoeuvre within a constrained optimization problem, successively varying its conditions in order to assess its cost in terms of the torque required to complete it.

4.2 Mathematical model

4.2.1 Details of the manoeuvre and reference frames

In the model, a spacecraft-based reference frame ("*body*"), centred in its centre of mass, is employed: the z-body axis of the satellite is considered as its optical axis, its x-body axis is the opposite direction vector to the one normal to the surface on which the solar array is placed, and the y-body axis to complete the right-hand triad. Figures 4.2 and 4.3 present a portrayal of this reference frame with respect to the Sun direction vector. The Sun-Earth synodic system, originating at the common centre of mass of the two bodies, is here approximated to a quasi-inertial reference frame with respect to the position of RAFTER. The point L2 around which RAFTER is expected to orbit therefore lies on the 'quasi-inertial' x-axis, which corresponds to the Sun-Earth-L2 conjunction.

Since a rotation around the z-body axis would result in RAFTER always observing the same stars, but rotated across the field of view, the basic manoeuvre that will be simulated is a 10-degree rotation in 20 minutes around the x-body axis or the y-body axis. These manoeuvres will then be repeated, alternating the rotation axes, to perform an entire scan. Additional simulations will vary the conditions in question, namely the axis of rotation, the angle of rotation, the duration of the manoeuvre and the method of solution to the optimization problem, which is presented in the next subsection.

4.2.2 Attitude constraints

Kinematics and dynamics constraints

In order to study and model its attitude dynamics and kinematics, in the present work the spacecraft is approximated by a rigid body. Its attitude dynamics is therefore described

by Euler's equation[46], namely:

$$I\dot{\omega} = \vec{u} - \vec{\omega} \times I\vec{\omega} \tag{4.1}$$

where $I = diag(I_x, I_y, I_z)$ is the **inertia tensor**, a diagonal matrix featuring the moments of inertia about the three principal axes of inertia of the spacecraft, $u = [u_x, u_y, u_z]^T$ is the three-axis **control torque** and $\omega = [\omega_x, \omega_y, \omega_z]^T$ represents the three-axis **angular velocity**[17].

In the context of the problem under consideration, it is assumed that the total torque exerted on the spacecraft, given by the first member of the Euler's equation, is a consequence of the control torque imparted to the system as well as a disturbance torque related to the environment in which it operates. Since RAFTER is orbiting Sun-Earth L2, at a distance of about $1.5 \cdot 10^6$ km from the Earth and $151.1 \cdot 10^6$ km from the Sun, the only external disturbance torque that could have a minimally relevant effect on the spacecraft attitude is the one related to the **solar radiation pressure**. In the present study, a simplified formulation is applied to estimate the order of magnitude and thus the potential effects on attitude variation. This torque is expressed as follows[49]:

$$\vec{T_S} = \vec{r_P} \times \vec{F_S} \tag{4.2}$$

with r_P as the distance vector from the center of mass of the spacecraft to its optical center of pressure, i.e. the lever arm of the solar radiation pressure force, F_S, expressed in body coordinate frame. Such a force is given as[49]:

$$F_S = (1 + K)P_S \cdot S \tag{4.3}$$

where $P_S = \frac{I_S}{c}$ is the proper *solar radiation pressure*, defined by the ratio between the **solar radiation flux** (approximately 1300 W/m^2 at the considered distance from the Sun) and the speed of light, S is the **spacecraft surface** perpendicular to the pressure force, which has a direction along the Sun-Earth-L2 axis, and K is its **reflectivity**, here set equal to 0.2. The solar pressure force is thus essentially constant at the distance involved, varying only with the area that the spacecraft faces from time to time towards the Sun.[49] The offset between the centre of mass and the optical centre of pressure of the spacecraft, r_P, is conservatively taken to be half the maximum length of said surface. The additional torque generated by the solar radiation pressure force and said misalignment results to have a component mainly around the y body axis of the satellite but, depending on its orientation, also around the z or x body axes. The direction of action of the solar pressure and its impact area, as well as a schematic of the body reference frame centred in the centre of mass of the spacecraft, are depicted in Figure 4.3.

The contribution of the solar radiation pressure torque is thereby added to the Euler equation of the system dynamics, which becomes

$$I\dot{\omega} = \vec{u} - \vec{T_S} - \vec{\omega} \times I\vec{\omega}. \tag{4.4}$$

In order to circumvent singularities and to reduce the computational cost, the spacecraft's attitude kinematics are analyzed utilizing quaternion $q = [q_0, q_1, q_2, q_3]^T$, with q_0 being the scalar part of the quaternion and $\vec{q_v} = [q_1, q_2, q_3]^T$ representing the vectorial part.[46, 17] The kinematics equation can be expressed as follows:

$$\dot{q} = \frac{1}{2}Q\vec{\omega} = \frac{1}{2}\vec{q}\Omega; \tag{4.5}$$

where

$$Q = \begin{bmatrix} -q_1 & -q_2 & -q_3 \\ q_0 & -q_3 & q_2 \\ q_3 & q_0 & -q_1 \\ -q_2 & q_1 & q_0 \end{bmatrix}$$

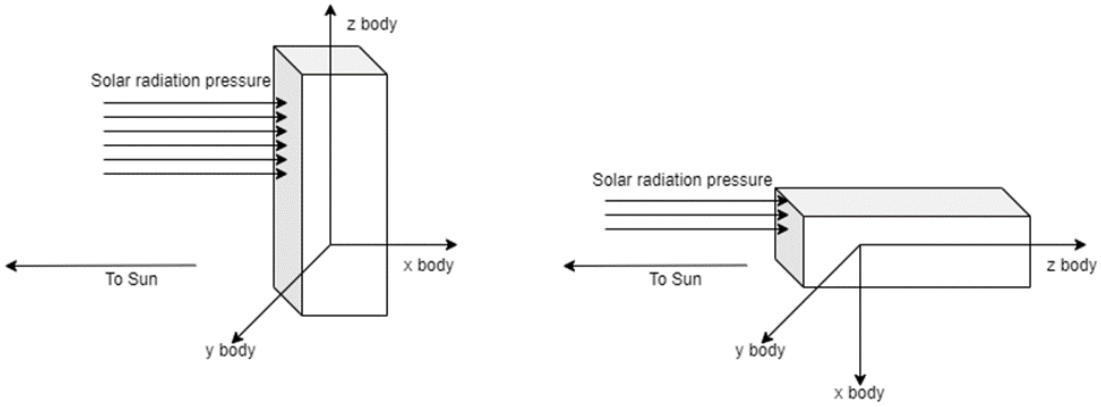

Figure 4.3: Direction of action of the solar pressure and impact area depending on the orientation of the satellite. When it is perpendicular to the y-z body plane it generates a torque around the y and z body axes, when it impacts on the x-y body plane the resulting torque has components along x and y body axes.

and

$$\Omega = \begin{bmatrix} 0 & -\omega_1 & -\omega_2 & -\omega_3 \\ \omega_1 & 0 & \omega_3 & -\omega_2 \\ \omega_2 & -\omega_3 & 0 & \omega_1 \\ \omega_3 & \omega_2 & -\omega_1 & 0 \end{bmatrix};$$

Rewriting the kinematics equation by making the scalar part and the vector part of the quaternion explicit yields[46]:

$$\dot{q}_0 = -\frac{1}{2}\vec{\omega}\vec{q_v} \tag{4.6}$$

and

$$\dot{q}_v = \frac{1}{2}(q_0\vec{\omega} - \vec{\omega} \times \vec{q_v}). \tag{4.7}$$

The attitude quaternion must comply with the normalization constraint $\|\vec{q}\|_2 = 1$[17].

Boundary constraints

Limitations on the maximum modulus of the control torque and angular velocity to be achieved by the spacecraft are additionally incorporated in the model in the form of *boundary constraints*[17], formulated as follows:

$$|u_i| \leq \gamma_T; \tag{4.8}$$

$$|\omega_i| \leq \omega_T; \tag{4.9}$$

with

$$i = 1, 2, 3.$$

The limitation on control input is contingent upon the fact that, in a real-world scenario, the applied torque is constrained to a finite value by the capacity of the actuating system designated to deliver it. In a similar fashion, the sensors on board the spacecraft detect the angular velocity within a specific range, limiting the maximum permissible amplitude therein[17].

Pointing constraints: forbidden and mandatory constraints

Forbidden constraints

One of the most critical pointing requirements is the prevention of the closest and brightest celestial bodies, such as the Sun, Earth and Moon, from entering the field of view of the optical instrument of RAFTER: this requirement results in a *forbidden constraint*. This constraint and the following mandatory constraint are translated into the model according to the approach employed by Wu and Han in their paper [17]. Referring to the Figure 4.4, r_B indicates the optical axis in a body reference frame, that is, in the case being considered, the body z-axis of the spacecraft, while r_I represents the direction vector, expressed in the inertial reference frame, of the celestial objects whose light is to be avoided by the system. In the problem at hand, this vector coincides with the Sun-Earth-L2 conjunction, i.e. the 'quasi-inertial' x-axis with the opposite sign. Although RAFTER is not located exactly at L2 but orbits it, the dimensions of any halo or Lissajous orbit would in any case be significantly smaller than the distance along the x-axis between the spacecraft and the centre of mass of the Sun-Earth system, so it is reasonable to approximate r_I as essentially parallel to the above-mentioned conjunction.

Defining θ as the solid half-angle of the cone within which r_B lies, it shall always be less than the angle between r_B and r_I for the constraint to be satisfied. Mathematically, this restriction can be stated as follows:

$$r_B^T(C_{BI}r_I) \leq cos\theta, \tag{4.10}$$

with $r_B = [r_{B_1}, r_{B_2}, r_{B_3}]^T$, $r_I = [r_1, r_2, r_3]^T$ and C_{BI} as the attitude cosine matrix of the spacecraft. The term in brackets can be rewritten by using the quaternion representation:

$$C_{BI}r_I = r_I - 2q_v^T q_v r_I + 2q_v q_v^T r_I + 2q_0(r_I \times q_v). \tag{4.11}$$

The equation 4.10 can be rewritten using a quadratic formulation:

$$q^T K_f q \leq 0 \tag{4.12}$$

with

$$K_f = \begin{bmatrix} r_I^T r_B - cos\theta & (r_B \times r_I^T)^T \\ r_B \times r_I^T & r_I r_B^T + r_B r_I^T - (r_I^T r_B + cos\theta)I \end{bmatrix}.$$

In the problem under study, θ is set equal to 90 degrees, which implies that the optical axis of the spacecraft is always located within the hemisphere that is opposite the direction of the Sun-Earth-L2 conjunction.

Mandatory constraints

A further requirement, which is equally pertinent, is the one defined by the *mandatory constraint*. In the context of this study, this is the imposition that the solar array of the spacecraft must face the Sun during the mission, and specifically during the observation manoeuvres. Going back to the Figure 4.4, v_B is defined as the normal direction vector to the surface on which the solar array is placed, given in a body reference frame. In the problem under discussion, it coincides with the negative x-axis in the body coordinate system, i.e. it is assumed that the solar array is placed on the back of the spacecraft. In a comparable and opposite manner to the case of forbidden constraint, here it is imposed that the angle between r_I and v_B shall always be less than a certain quantity, called λ, which represents the half-amplitude of the solid angle in which v_B must always lie, i.e.:

$$v_B^T(C_{BI}r_I) \geq cos\lambda. \tag{4.13}$$

Rearranging and applying the quadratic formulation, the following is obtained:

$$q^T K_m q \geq 0, \tag{4.14}$$

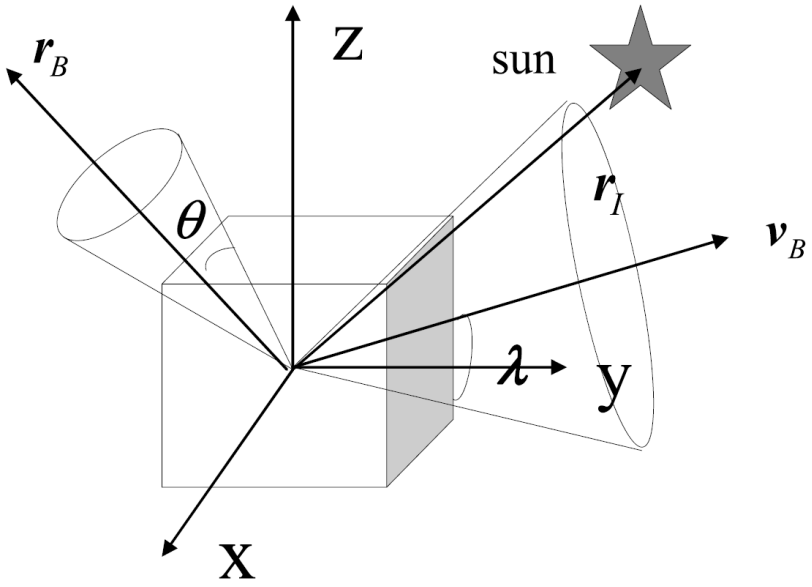

Figure 4.4: Pointing constraints.[17]

where

$$K_m = \begin{bmatrix} r_I^T v_B - cos\theta & (v_B \times r_I^T)^T \\ v_B \times r_I^T & r_I v_B^T + v_B r_I^T - (r_I^T v_B + cos\theta) I \end{bmatrix}.$$

In the practical case of this thesis, the selected λ value is 120 degrees, imposing that the normal direction vector to the solar array is always contained within a solid angle of 240° within which lies the direction of the Sun-Earth-L2 conjunction.

4.2.3 Problem statement

The aim of the study is to generate an energy-optimal attitude manoeuvring path which shall satisfy the above-mentioned attitude, boundary and pointing constraints. Having thus assigned the initial and final attitude and angular velocities, the objective of the analysis is to minimize the integral over time of a certain cost function associated with the energy of the studied manoeuvre. In this specific instance, the selected cost functions are the square of the input torque applied to the spacecraft and the absolute value of said input torque: the former will result in a control torque with a continuous and generally linear behaviour, whereas the latter will lead to a torque delivered at its maximum value only at the beginning and (opposite in sign) at the end of the manoeuvre, following a criterion similar to a *bang-bang controller*.

The optimal control problem, subject to the constraints outlined above, can be formulated as follows:

$$min : J = \int_{t_0}^{t_f} u^2(t)\, dt$$

or

$$min : J = \int_{t_0}^{t_f} |u(t)|\, dt$$

s.t.

$$\begin{cases} I\dot{\omega} = \vec{u} - \vec{T_S} - \vec{\omega} \times I\vec{\omega} & \text{(dynamic constraints)} \\ \dot{q} = \frac{1}{2}Q\vec{\omega} = \frac{1}{2}\vec{q}\Omega & \text{(kinematic constraints)} \\ -\gamma_T \leq u_i \leq \gamma_T, i = 1,2,3 & \text{(boundary constraints)} \\ -\omega_T \leq \omega_i \leq \omega_T, i = 1,2,3 & \text{(boundary constraints)} \\ q(t)^T K_f q(t) \leq 0 & \text{(forbidden constraints)} \\ q(t)^T K_m q(t) \geq 0 & \text{(mandatory constraints)} \\ q(t)^T q(t) = 1 & \text{(normalisation constraints)} \\ q(t_0) = q_0, \omega(t_0) = \omega_0 & \text{(initial conditions)} \\ q(t_f) = q_f, \omega(t_f) = \omega_f & \text{(terminal conditions)} \end{cases} \tag{4.15}$$

What is stated above is a **nonlinear programming problem**. In order to solve it, the open-source MATLAB library **OptimTraj**, developed by Dr. Matthew Peter Kelly [13], has been exploited. The library is designed to solve continuous-time single-phase trajectory optimization problems, is based on the MATLAB function *fmincon* and allows three direct optimization methods to be selected and applied: the **trapezoidal direct collocation** method, the **Hermite-Simpson direct collocation** method and the **Runge-Kutta** 4^{th} **order direct multiple shooting** method.

Slack variables

In the second formulation of the problem, the discontinuity resulting from the use of the absolute value of the control torque in the objective function is handled by employing slack variables, thus moving the discontinuity to a set of constraints, where the nonlinear programming solver can properly manage it.

The methodology adopted here is the one mentioned in Kelly's [13] paper. First, the objective function is rewritten by introducing two (arrays of) slack variables, named s_1 and s_2:

$$min : J = \int_{t_0}^{t_f} |u(t)|\, dt \longrightarrow min : J = \int_{t_0}^{t_f} (s_1(t) + s_2(t))\, dt \tag{4.16}$$

Further constraints are then imposed:

- the slack variable shall be positive, i.e.

$$0 \leq s_1(t), 0 \leq s_2(t) \tag{4.17}$$

- the difference between the slack variables shall be equal to the term inside the *abs()* function, i.e.

$$s_1(t) - s_2(t) = u(t). \tag{4.18}$$

The set of constraints presented thus far fundamentally defines $s_1(t)$ as the positive part of the argument of the absolute value function and $s_2(t)$ as the magnitude of the negative part. Said modifications render the problem suitable for input into a nonlinear programming solver.

Chapter 5

Simulation results

This Chapter summarizes and discusses the results of the simulations carried out to solve the constrained optimization problem presented in Chapter 4. The manoeuvre is simulated for both spacecraft configurations and utilizing both cost functions. The simulation conditions are shown in Table 5.1.

Initial quaternions q^0	[1 0 0 0]'
Final quaternions q^f	q_1^f = [0.9962 0.0872 0 0]' (+10° about x body axis) q_2^f = [0.9962 -0.0872 0 0]' (-10° about x body axis) q_3^f = [0.9962 0 0.0872 0]' (+10° about y body axis) q_4^f = [0.9962 0 -0.0872 0]' (-10° about y body axis) q_5^f = [0.9990 0.0436 0 0]' (+5° about x body axis) q_6^f = [0.9914 0.1305 0 0]' (+15° about x body axis) q_7^f = [0.9990 0 0.0436 0]' (+5° about y body axis) q_8^f = [0.9914 0 0.1305 0]' (+15° about y body axis)
Initial angular velocities ω_0	[0 0 0]'
Final angular velocities ω_f	[0 0 0]'
Initial guess torques u_0	[0 0 0]'
Max angular velocity ω_T	0.05 rad/s [17]
Max torque γ_T	$\gamma_{T_1} = 1$ Nm $\gamma_{T_2} = 5 \cdot 10^{-4}$ Nm $\gamma_{T_3} = 5 \cdot 10^{-6}$ Nm

Table 5.1: Simulation conditions.

Both rotation around the x-axis and the y-axis, in both positive and negative directions, have been simulated. The manoeuvre time dictated by the mission requirements is 20 minutes (1200 seconds). Subsequently, each rotation has been repeated in two scenarios: one in which the solar radiation pressure is normal to the y-z body plane and one in which it is perpendicular to the x-y body plane. This has been done to account for the fact that the surface facing the Sun is smaller when the spacecraft is oriented such that the solar pressure is perpendicular to the x-y body plane, therefore the solar radiation pressure torque itself has a lower magnitude.

Afterwards, a parametric analysis has been conducted only for the manoeuvre which, of those listed above, has turned out to be the most expensive in terms of the control torque obtained. In particular, manoeuvre time and rotation angle have been parameterized, respectively, as follows: 15 minutes (900 seconds), 20 minutes (1200 seconds), 25 minutes

(1500 seconds), and 5°, 10° and 15°. From this parametric analysis, it is intuitive to expect an increment in control torque as the required manoeuvring time decreases and the imposed angle of rotation increases, although it remains within the same order of magnitude.

A further study has been carried out to ascertain the impact of the maximum allowable torque γ_T, as constrained by boundary conditions, on the system behaviour and overall results. For the nominal configuration, a value of γ_T equal to 1 Nm and 10^{-4} Nm has been adopted, while for the Cubesat configuration the maximum allowable torque has been set equal to 1 Nm and 10^{-6} Nm.

The most significant plots in relation to system behaviour are provided for each case.

5.1 Nominal ("Euclid-like") case

In this case, the z-axis, i.e. the optical axis, is also the axis of minimum inertia: in the absence of the effects of solar radiation pressure, the torques around the x-axis and around the y-axis would be identical in each condition. The x-y body plane of the spacecraft has a smaller surface area than the y-z plane, which results in a greater value for solar radiation pressure in the latter case. In particular, with reference to Equation 4.2, the value is $1.5611 \cdot 10^{-5}$ Nm when the vector is perpendicular to the x-y body plane and $8.7811 \cdot 10^{-5}$ Nm when it is perpendicular to the y-z body plane.

5.1.1 Optimization of u^2

The results obtained by optimizing the input torque-squared by using the Hermite-Simpson direct collocation are presented. For each simulation, the behaviour is identical: a positive but decreasing linear torque is applied, which causes the spacecraft to accelerate to a maximum angular velocity of approximately $2.2 \cdot 10^{-4}$ rad/s, which is reached when the torque becomes zero. Subsequently, the torque turns negative and continues to decrease, while the angular velocity begins to decrease until it returns to zero. The angular velocity curve is parabolic, as its derivative is proportional to the applied torque, which in this case is linear. This relationship is expressed by the Euler's Equation 4.1.

The behaviour outlined above is illustrated in Figure 5.1, which depicts the plots of angular velocities, quaternions and applied torques for a positive rotation of 10 degrees around the x-axis, over a 20-minute period, and is observed, with slightly different values, for all simulations performed in this case. These results indicate that a relatively small and precisely controlled torque is continuously delivered throughout the duration of the manoeuvre. The maximum control torque is about $\sim 4.8 - 5.0 \cdot 10^{-4}$ Nm, the greatest value being observed at rotations around the y-axis, due to the additional contribution of the solar radiation pressure. This axis has therefore been selected to simulate parametric rotations as the manoeuvring time and angle of rotation change. The results of this analysis are presented in Table 5.2.

It has been noticed that the same order of magnitude for the maximum control torque is reached whether a value of γ_T equal to 1 Nm or $5 \cdot 10^{-4}$ Nm is imposed.

The results described so far have been obtained by adopting Hermite-Simpson direct collocation as the optimization method, discretizing the trajectory into 50 segments. Further simulations have been carried out by employing trapezoidal direct collocation (50-point grid) and Runge-Kutta multiple shooting (50 segments). In any case, it can be remarked that the values remain highly consistent, indicating that the local minimum identified by the code at each simulation may also be a global minimum.

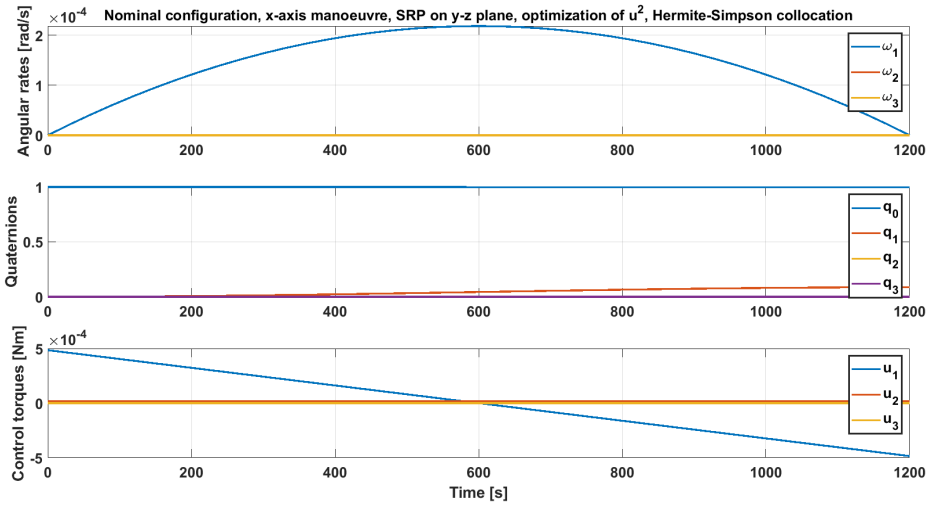

Figure 5.1: Plots of angular velocities, quaternions and control torques for a positive rotation of 10 degrees around the x-axis in 20 minutes, when the solar pressure is acting in the y-z body plane and therefore gives a non-zero component to the torque about the y-axis, obtained for the nominal configuration by optimizing u^2.

	900 s	**1200 s**	**1500 s**
5°	**Cost function** $5.5934 \cdot 10^{-5}$ **Max torque** $4.4655 \cdot 10^{-4}$ Nm **Min torque** $-4.1533 \cdot 10^{-4}$ Nm	**Cost function** $2.3797 \cdot 10^{-5}$ **Max torque** $2.5806 \cdot 10^{-4}$ Nm **Min torque** $-2.2684 \cdot 10^{-4}$ Nm	**Cost function** $1.2400 \cdot 10^{-5}$ **Max torque** $1.7088 \cdot 10^{-4}$ Nm **Min torque** $-1.3966 \cdot 10^{-4}$ Nm
10°	**Cost function** $2.2308 \cdot 10^{-4}$ **Max torque** $8.7750 \cdot 10^{-4}$ Nm **Min torque** $-8.4628 \cdot 10^{-4}$ Nm	**Cost function** $9.4310 \cdot 10^{-5}$ **Max torque** $5.0047 \cdot 10^{-4}$ Nm **Min torque** $-4.6924 \cdot 10^{-4}$ Nm	**Cost function** $4.8503 \cdot 10^{-5}$ **Max torque** $3.2602 \cdot 10^{-4}$ Nm **Min torque** $-2.9480 \cdot 10^{-4}$ Nm
15°	**Cost function** $5.0165 \cdot 10^{-4}$ **Max torque** $1.3085 \cdot 10^{-3}$ Nm **Min torque** $-1.2773 \cdot 10^{-3}$ Nm	**Cost function** $2.1183 \cdot 10^{-4}$ **Max torque** $7.4273 \cdot 10^{-4}$ Nm **Min torque** $-7.1154 \cdot 10^{-4}$ Nm	**Cost function** $1.0867 \cdot 10^{-4}$ **Max torque** $4.8100 \cdot 10^{-4}$ Nm **Min torque** $-4.4997 \cdot 10^{-4}$ Nm

Table 5.2: Cost function (i.e. integral of u^2) and maximum and minimum applied torque values for a field-of-view rotation manoeuvre of 5, 10 and 15 degrees about the y-axis in 15, 20 and 25 minutes, considering the nominal configuration.

5.1.2 Optimization of $|u|$

The manoeuvres described at the outset of this Chapter have also been simulated by utilizing the integral over time of the absolute value of the control torque as a cost function. In this instance, the selected optimization method is the trapezoidal direct collocation,

considering a 100-point discretization grid. Nevertheless, to confirm the consistency of certain results, several simulations have been repeated using the Hermite-Simpson collocation, discretizing the trajectory in 50 segments. Simulations have first been carried out by imposing a maximum allowable torque value γ_T equal to 1 Nm and then, in order to compare its behaviour with the u^2 optimization case, by employing a limit value of $5 \cdot 10^{-4}$ Nm (equivalent to the maximum value obtained for the same configuration but optimizing the square of the control torque).

In the case where γ_T in equal to 1 Nm, the behaviour of the quantities involved is essentially similar for each simulation, as illustrated in Figure 5.2. At the start of the manoeuvre, a positive 'quasi-impulsive' torque is delivered, which rapidly increases the angular velocity to a constant value of about $15 \cdot 10^{-5}$ rad/s reached when the torque returns to zero. The satellite will rotate with said constant angular velocity until it reaches the desired attitude, at which point an equal and opposite torque will be applied to stop the rotation. The magnitude of the applied torques is approximately $10^{-2} - 10^{-3}$ Nm (depending on the number of segments in which the trajectory is discretized), which is considerably larger than the values obtained by optimizing the square of the input torque.

Figure 5.3 depicts an exemplar of the system behaviour in the event when the maximum allowable torque γ_T is set equal to $5 \cdot 10^{-4}$ Nm. When the manoeuvre initiates, a positive torque is delivered and, for over 200 seconds, is held at its maximum value - of the same order of magnitude of γ_T, as expected -, time during which it increases the angular velocity up to a constant value of about $18 \cdot 10^{-5}$ rad/s, reached when the torque returns to zero. The satellite will reorient itself with the above-mentioned constant angular velocity until it approaches the desired attitude, when an equal and opposite torque will be applied to slowly stop the rotation.

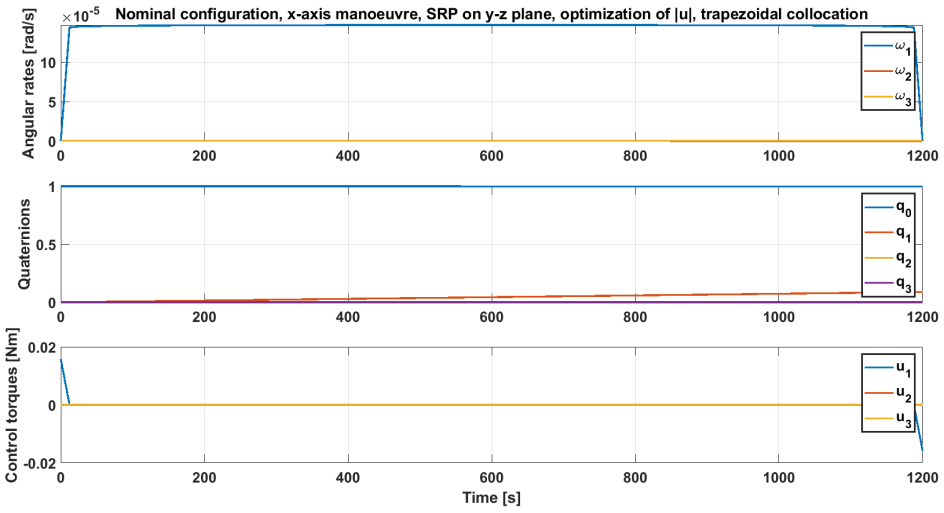

Figure 5.2: Plots of angular velocities, quaternions and control torques for a positive rotation of 10 degrees around the x-axis in 20 minutes, when the solar pressure is acting in the y-z body plane, obtained for the nominal configuration by optimizing $|u|$ and setting a γ_T value of 1 Nm.

When the solar radiation pressure torque acts around the selected axis of rotation, however, the torque required to initiate the manoeuvre and the final torque to stop the motion will no longer be equal in magnitude. Rather, one will be slightly greater than the other, depending on the direction of the solar radiation pressure torque. In the

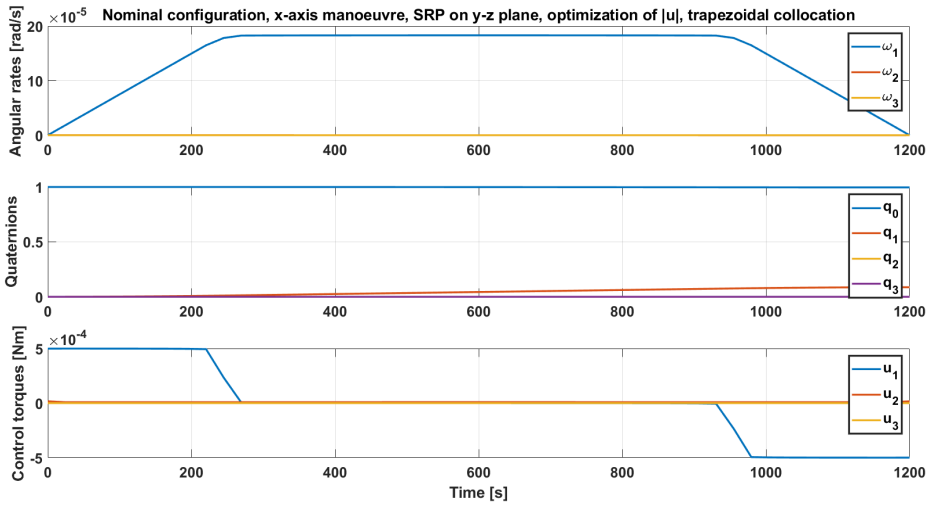

Figure 5.3: Plots of angular velocities, quaternions and control torques for a positive rotation of 10 degrees around the x-axis in 20 minutes, when the solar pressure is acting in the y-z body plane, obtained for the nominal configuration by optimizing $|u|$ and setting a γ_T value of $5 \cdot 10^{-4}$ Nm.

event that the direction is negative, indicating a braking effect of the solar pressure, the angular velocity will slowly decrease during the operation and the initial control torque will be slightly larger in order to counteract the disturbance and complete the manoeuvre. Conversely, the final torque will be smaller since the satellite will have already partially slowed down during its rotation. This behaviour can be observed in Figure 5.4 and in Figure 5.5 in the case of γ_T equal to 1 Nm and to $5 \cdot 10^{-4}$ Nm respectively. The opposite behaviour is observed when the solar radiation pressure torque direction is positive.

If the Hermite-Simpson direct collocation method is employed, the achieved control torque result typically slightly higher than that obtained using the trapezoidal collocation, as the angular velocity reaches a small peak before settling at its constant manoeuvring value, as can be seen in Figure 5.6.

Table 5.3 displays the results of the parameterization of rotation angles and manoeuvre times, considering as the rotation axis the x-axis body in the case of solar radiation pressure perpendicular to the x-y plane, namely the condition in which the torque is at its greatest, due to the influence of solar radiation pressure.

On the other hand, Table 5.4 displays the results obtained by parameterising the manoeuvring time and angle of rotation for the same conditions as above, but in the case where the maximum allowable torque value γ_T is set equal to $5 \cdot 10^{-4}$ Nm. It is noteworthy that the maximum torque hovers around similar values across all simulations, despite variations in the cost function: this is easily understood by imagining that for each simulation result the only significantly varying quantity is the duration over which the maximum torque is mantained constant at the beginning and end of the manoeuvre. The simulations of the 10° and 15° rotations in 900 s (15 minutes), while converging, fail to satisfy all the imposed constraints: the torque required to execute the manoeuvre under these conditions is greater than $5 \cdot 10^{-4}$ Nm, due to the shorter time required (and therefore the higher necessary angular velocity) and the greater magnitude of the manoeuvring angles.

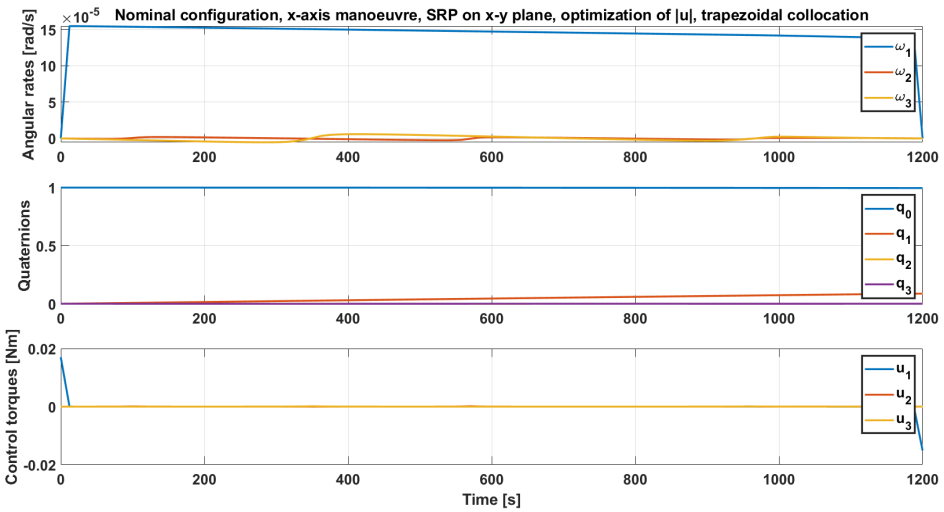

Figure 5.4: Plots of angular velocities, quaternions and control torques for a positive rotation of 10 degrees around the x-axis in 20 minutes, when the solar pressure is acting in the x-y body plane, obtained for the nominal configuration by optimizing $|u|$ and setting a γ_T value of 1 Nm.

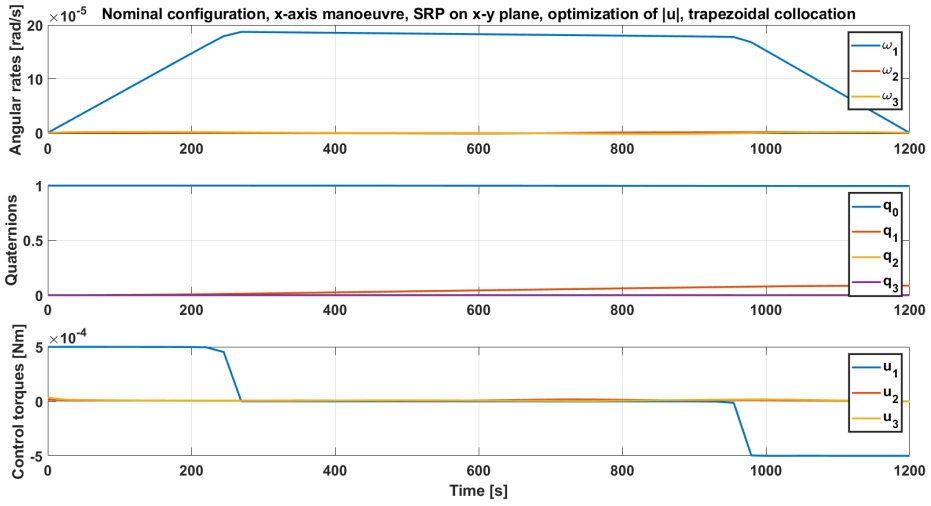

Figure 5.5: Plots of angular velocities, quaternions and control torques for a positive rotation of 10 degrees around the x-axis in 20 minutes, when the solar pressure is acting in the x-y body plane, obtained for the nominal configuration by optimizing $|u|$ and setting a γ_T value of $5 \cdot 10^{-4}$ Nm.

5.2 CubeSat 18U case

In this instance, the dimensions of the x-axis and y-axis are not identical, therefore the control torque around y-axis will result to be slightly different from that around x, both because the latter is the axis of maximum inertia and because the solar radiation pressure torque is consistently oriented around the y-axis, once more giving a more significant contribution in that direction. In this case, the x-y plane and the y-z plane have the same dimensions and the solar radiation pressure torque has a value of $4.6832 \cdot 10^{-8}$ Nm.

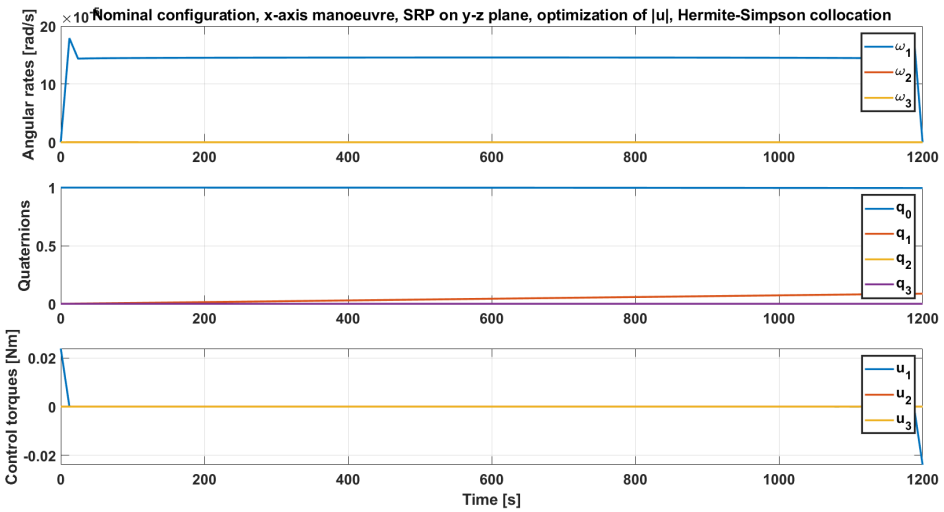

Figure 5.6: Plots of angular velocities, quaternions and control torques for a positive rotation of 10 degrees around the x-axis in 20 minutes, when the solar pressure is acting in the x-y body plane, obtained for the nominal configuration by optimizing $|u|$ employing Hermite-Simpson collocation and setting a γ_T value of 1 Nm.

	900 s	**1200 s**	**1500 s**
5°	**Cost function** 0.1472 **Max torque** 0.0151 Nm **Min torque** -0.0134 Nm	**Cost function** 0.1198 **Max torque** 0.0089 Nm **Min torque** -0.0071 Nm	**Cost function** 0.1055 **Max torque** 0.0060 Nm **Min torque** -0.0042 Nm
10°	**Cost function** 0.2781 **Max torque** 0.0294 Nm **Min torque** -0.0278 Nm	**Cost function** 0.2179 **Max torque** 0.0170 Nm **Min torque** -0.0151 Nm	**Cost function** 0.1858 **Max torque** 0.0104 Nm **Min torque** -0.0088 Nm
15°	**Cost function** 0.4088 **Max torque** 0.0440 Nm **Min torque** -0.0414 Nm	**Cost function** 0.3288 **Max torque** 0.0236 Nm **Min torque** -0.0219 Nm	**Cost function** 0.2641 **Max torque** 0.0162 Nm **Min torque** -0.0145 Nm

Table 5.3: Cost function (i.e. integral of $|u|$) and maximum and minimum applied torque values for a field-of-view rotation manoeuvre of 5, 10 and 15 degrees about the x-axis in 15, 20 and 25 minutes, considering the nominal configuration and a γ_T value of 1 Nm.

5.2.1 Optimization of u^2

The results of simulations undertaken by minimizing the square of the input torque for the CubeSat configuration are discussed here. The methodologies adopted and the considerations drawn are essentially analogous to those for the nominal configuration

	900 s	**1200 s**	**1500 s**
5°	**Cost function** 0.1732 **Max torque** $4.9890 \cdot 10^{-4}$ Nm **Min torque** $-4.9890 \cdot 10^{-4}$ Nm	**Cost function** 0.1278 **Max torque** $4.9732 \cdot 10^{-4}$ Nm **Min torque** $-4.9732 \cdot 10^{-4}$ Nm	**Cost function** 0.1082 **Max torque** $4.9639 \cdot 10^{-4}$ Nm **Min torque** $-4.9640 \cdot 10^{-4}$ Nm
10°	**Converges at infeasible point**	**Cost function** 0.2649 **Max torque** $4.9934 \cdot 10^{-4}$ Nm **Min torque** $-4.9934 \cdot 10^{-4}$ Nm	**Cost function** 0.2020 **Max torque** $4.9878 \cdot 10^{-4}$ Nm **Min torque** $-4.9878 \cdot 10^{-4}$ Nm
15°	**Converges at infeasible point**	**Cost function** 0.5179 **Max torque** $4.9990 \cdot 10^{-4}$ Nm **Min torque** $-4.9990 \cdot 10^{-4}$ Nm	**Cost function** 0.3142 **Max torque** $4.9938 \cdot 10^{-4}$ Nm **Min torque** $4.9938 \cdot 10^{-4}$ Nm

Table 5.4: Cost function (i.e. integral of $|u|$) and maximum and minimum applied torque values for a field-of-view rotation manoeuvre of 5, 10 and 15 degrees about the x-axis in 15, 20 and 25 minutes, considering the nominal configuration and a γ_T value of $5 \cdot 10^{-4}$ Nm.

reasoned in Subsection5.1.1. In this instance, as with the nominal configuration, simulations have initially been performed by imposing a γ_T value of 1 Nm and applying the Hermite-Simpson method with a 50-segment discretization. Subsequently, following the study of the orders of magnitude obtained for the control torque and the behaviour of the system, the analysis has then been repeated by setting a torque limit value of $5 \cdot 10^{-6}$ Nm and selecting the trapezoidal direct collocation with a 50-point grid as the optimization method. The Runge-Kutta method has been applied on occasion to corroborate the consistency of results, with each application yielding outcomes analogous to those obtained through the Hermite-Simpson collocation.

For the case when γ_T is set equal to 1 Nm, the principal distinction from the nominal configuration case, apart from the smaller order of magnitude of the control torques (around 10^{-6} Nm) due to the reduced inertia of this configuration, is observed in the behaviour of the quantities at stake, as illustrated in Figure 5.7. In this scenario, a small torque is provided at the start of the manoeuvre, which causes the spacecraft to accelerate until, following a short transient period, it reaches an almost constant angular velocity of approximately $15 \cdot 10^{-5}$ rad/s, with which it will rotate to orient itself with the desired attitude. Once this value is reached, the angular velocity will oscillate around it, while the torque will fluctuate close to zero, then decrease at the end of the manoeuvre to slow the body down again.

Table 5.5 displays the results of the parameterization of rotation angles and manoeuvre times, considering as the rotation axis the y body axis, around which the ever-present contribution of solar radiation pressure intensifies the magnitude of the maximum torque obtained.

Given the expectation of similar behaviour to the nominal configuration case, which

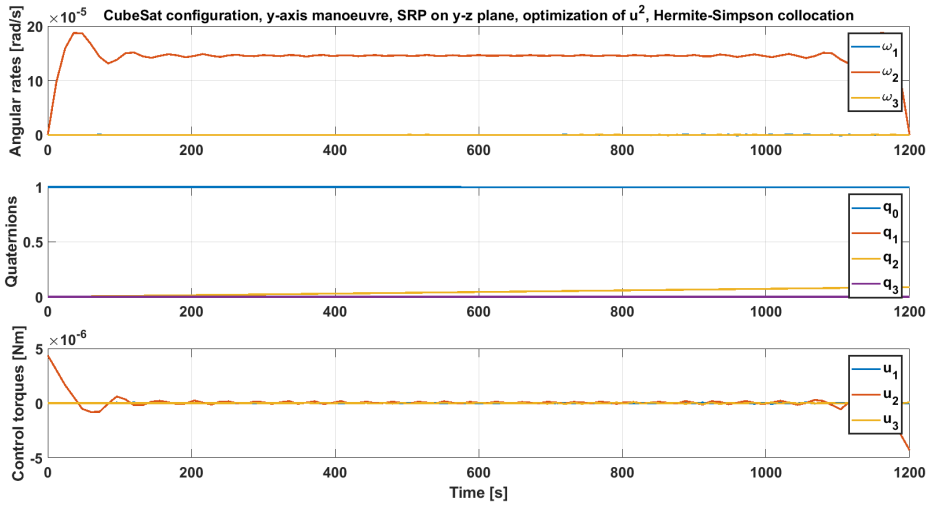

Figure 5.7: Plots of angular velocities, quaternions and control torques for a positive rotation of 10 degrees around the y-axis in 20 minutes, when the solar pressure is acting in the y-z body plane, obtained for the CubeSat configuration by optimizing u^2 and considering a γ_T value of 1 Nm.

	900 s	**1200 s**	**1500 s**
5°	**Cost function** $3.4932 \cdot 10^{-10}$ **Max torque** $4.0514 \cdot 10^{-6}$ Nm **Min torque** $-3.9520 \cdot 10^{-6}$ Nm	**Cost function** $1.9047 \cdot 10^{-10}$ **Max torque** $2.9153 \cdot 10^{-6}$ Nm **Min torque** $-2.8211 \cdot 10^{-6}$ Nm	**Cost function** $1.0774 \cdot 10^{-10}$ **Max torque** $1.9523 \cdot 10^{-6}$ Nm **Min torque** $-1.8701 \cdot 10^{-6}$ Nm
10°	**Cost function** $8.7215 \cdot 10^{-10}$ **Max torque** $5.1618 \cdot 10^{-6}$ Nm **Min torque** $-5.0822 \cdot 10^{-6}$ Nm	**Cost function** $4.7995 \cdot 10^{-10}$ **Max torque** $3.7953 \cdot 10^{-6}$ Nm **Min torque** $-3.7413 \cdot 10^{-6}$ Nm	**Cost function** $3.2632 \cdot 10^{-10}$ **Max torque** $3.1453 \cdot 10^{-6}$ Nm **Min torque** $-3.1232 \cdot 10^{-6}$ Nm
15°	**Cost function** $1.7396 \cdot 10^{-9}$ **Max torque** $6.9445 \cdot 10^{-6}$ Nm **Min torque** $-6.8734 \cdot 10^{-6}$ Nm	**Cost function** $9.4135 \cdot 10^{-10}$ **Max torque** $5.0221 \cdot 10^{-6}$ Nm **Min torque** $-4.9338 \cdot 10^{-6}$ Nm	**Cost function** $6.1770 \cdot 10^{-10}$ **Max torque** $4.1282 \cdot 10^{-6}$ Nm **Min torque** $-4.0253 \cdot 10^{-6}$ Nm

Table 5.5: Cost function (i.e. integral of u^2) and maximum and minimum applied torque values for a field-of-view rotation manoeuvre of 5, 10 and 15 degrees about the y-axis in 15, 20 and 25 minutes, considering the CubeSat configuration and a γ_T value of 1 Nm.

is however not observed here, a further analysis has been proposed and performed. In this additional study, the value of the maximum allowable torque, γ_T, has been reduced to the same order of magnitude the maximum control torque that has been achieved thus far, having assigned it a value of $5 \cdot 10^{-6}$ Nm. This novel approach results - as expected - in a smaller order of magnitude of the torques (around 10^{-7} Nm). In this instance,

prior to assuming the - previously observed for the nominal configuration case - linear behaviour, the control torque undergoes a brief increase to a maximum at the beginning of the manoeuvre, and again at the end of the rotation, as illustrated in Figure 5.8. The presence of solar radiation pressure (if negative in direction, as discussed here) results in a shift of the control torque curve to the right, which will no longer change sign at mid-manoeuvre, but about 100 seconds later: this behaviour can be observed in Figure 5.9.

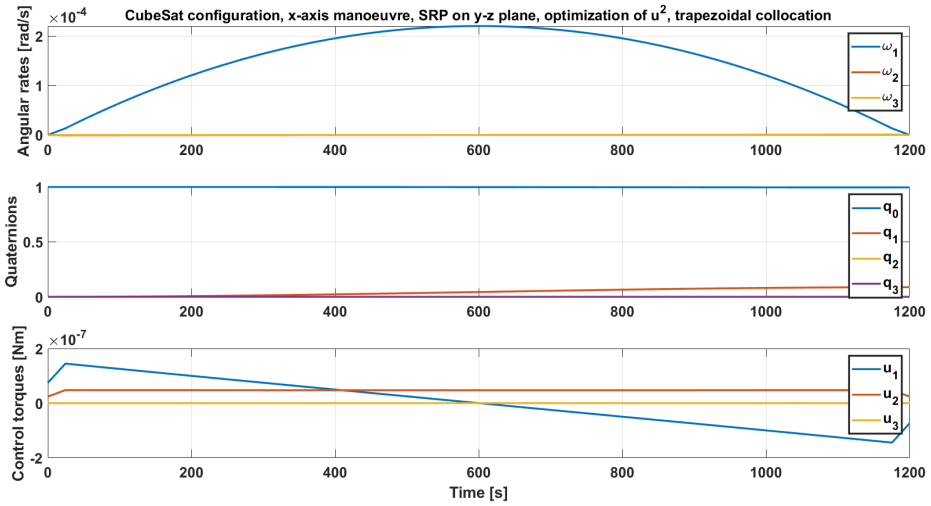

Figure 5.8: Plots of angular velocities, quaternions and control torques for a positive rotation of 10 degrees around the x-axis in 20 minutes, when the solar pressure is acting in the y-z body plane and therefore gives a non-zero component to the torque about the y-axis, obtained for the CubeSat configuration by optimizing u^2 and considering a γ_T value of $5 \cdot 10^{-6}$ Nm.

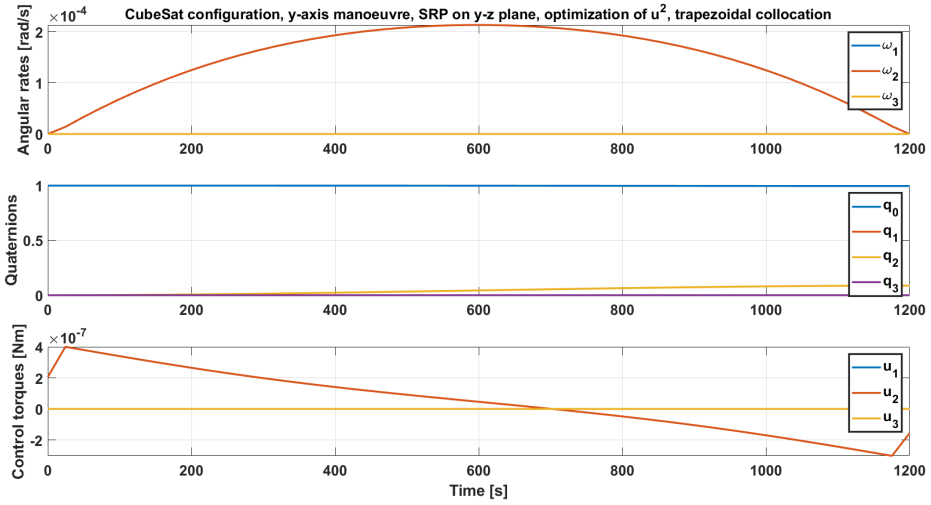

Figure 5.9: Plots of angular velocities, quaternions and control torques for a positive rotation of 10 degrees around the y-axis in 20 minutes, when the solar pressure is acting in the y-z body plane, obtained for the CubeSat configuration by optimizing u^2 and considering a γ_T value of $5 \cdot 10^{-6}$ Nm.

Table 5.6 displays the results of the parameterization of rotation angles and manoeuvre times, selected because of the markedly elevated magnitude of the torque resulting from the effects of solar radiation pressure, the influence of which can also be appreciated in Figure 5.9.

	900 s	**1200 s**	**1500 s**
5°	**Cost function** $2.7773 \cdot 10^{-11}$ **Max torque** $3.4414 \cdot 10^{-7}$ Nm **Min torque** $-2.4675 \cdot 10^{-7}$ Nm	**Cost function** $1.3560 \cdot 10^{-11}$ **Max torque** $2.2484 \cdot 10^{-7}$ Nm **Min torque** $-1.2655 \cdot 10^{-7}$ Nm	**Cost function** $9.0141 \cdot 10^{-12}$ **Max torque** $1.7341 \cdot 10^{-7}$ Nm **Min torque** $-7.4731 \cdot 10^{-8}$ Nm
10°	**Cost function** $1.0514 \cdot 10^{-10}$ **Max torque** $6.3450 \cdot 10^{-7}$ Nm **Min torque** $-5.3840 \cdot 10^{-7}$ Nm	**Cost function** $4.6303 \cdot 10^{-11}$ **Max torque** $4.0089 \cdot 10^{-7}$ Nm **Min torque** $-3.0273 \cdot 10^{-7}$ Nm	**Cost function** $2.6132 \cdot 10^{-11}$ **Max torque** $2.9805 \cdot 10^{-7}$ Nm **Min torque** $-1.9942 \cdot 10^{-7}$ Nm
15°	**Cost function** $2.3403 \cdot 10^{-10}$ **Max torque** $9.2562 \cdot 10^{-7}$ Nm **Min torque** $-8.3052 \cdot 10^{-7}$ Nm	**Cost function** $1.0087 \cdot 10^{-10}$ **Max torque** $5.7077 \cdot 10^{-7}$ Nm **Min torque** $-4.7374 \cdot 10^{-7}$ Nm	**Cost function** $5.4202 \cdot 10^{-11}$ **Max torque** $4.2232 \cdot 10^{-7}$ Nm **Min torque** $-3.1679 \cdot 10^{-7}$ Nm

Table 5.6: Cost function (i.e. integral of u^2) and maximum and minimum applied torque values for a field-of-view rotation manoeuvre of 5, 10 and 15 degrees about the y-axis in 15, 20 and 25 minutes, considering the CubeSat configuration and a γ_T value of $5 \cdot 10^{-6}$ Nm.

5.2.2 Optimization of $|u|$

The simulated conditions are analogous to those presented for the nominal configuration in the case discussed in Subsection 5.1.2. The order of magnitude of the torque applied is 10^{-6} Nm for both the considered γ_T values, due to the reduced envelope of the CubeSat. In this instance, the maximum input torque magnitude remains below the maximum allowable value γ_T and therefore decreases from the very beginning of the manoeuvre, i.e. it is not kept constant in the first and last moments of the operation, as depicted in Figure 5.10. In this scenario, the numerical outcomes achieved are relatively comparable to those attained for the analogous configuration through the optimization of the square of the torque. The value of the angular velocity reached is substantially comparable to that found in the previously discussed cases, namely $15 \cdot 10^{-5}$ rad/s.

Utilizing the Hermite-Simpson collocation, the same peak in angular velocity at the beginning and end of the manoeuvre is found as in the nominal configuration case, resulting in a marginally greater torque, as can be noted in Figure 5.11. This is the method implemented to parameterize the basic manoeuvre by varying its duration and angle of rotation, both because of the higher torques involved, which can provide more dimensioning values, and because it is the method that has demonstrated the most consistent results. The results of these simulations are shown in Table 5.7. The parameterised rotation is

the one around the x body axis in the condition where the solar radiation pressure is perpendicular to the y-z plane.

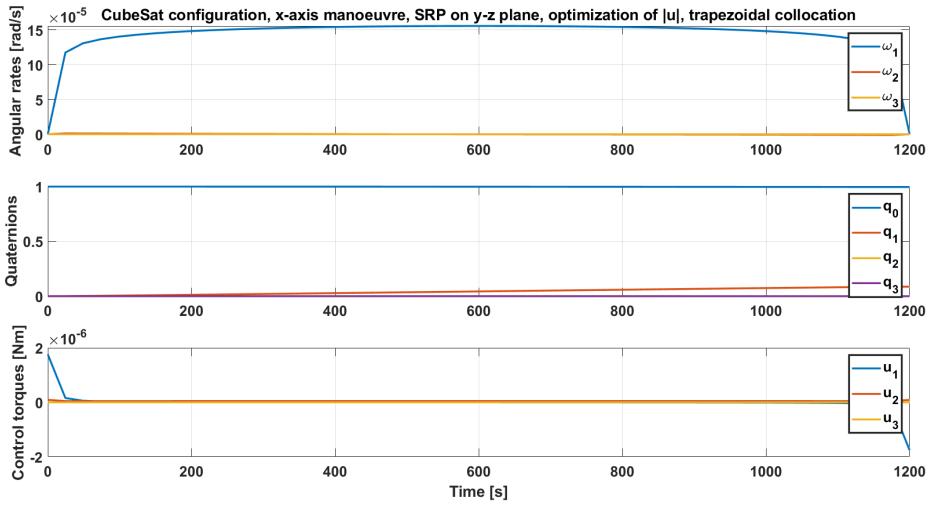

Figure 5.10: Plots of angular velocities, quaternions and control torques for a positive rotation of 10 degrees around the x-axis in 20 minutes, when the solar pressure is acting in the y-z body plane, obtained for the CubeSat configuration by optimizing $|u|$ with the trapezoidal collocation method.

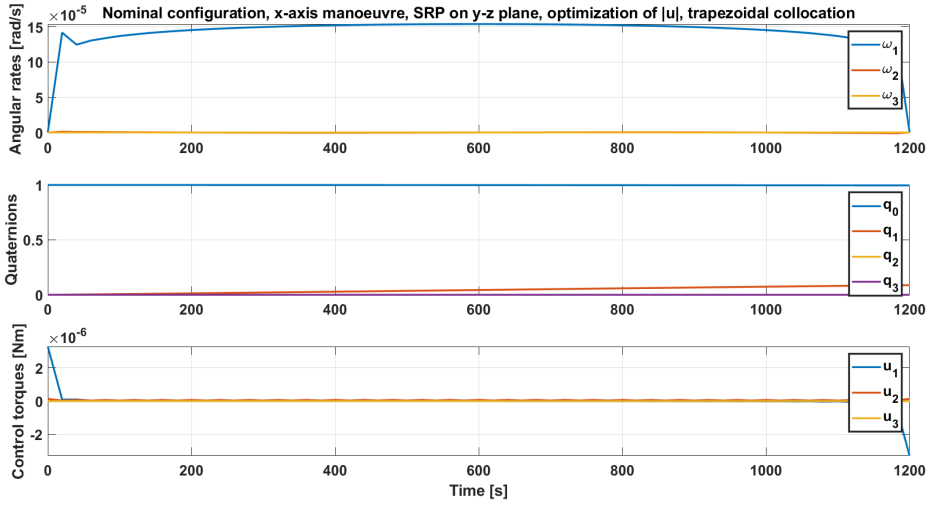

Figure 5.11: Plots of angular velocities, quaternions and control torques for a positive rotation of 10 degrees around the x-axis in 20 minutes, when the solar pressure is acting in the y-z body plane, obtained for the CubeSat configuration by optimizing $|u|$ with the Hermite-Simpson collocation method.

	900 s	**1200 s**	**1500 s**
5°	**Cost function** $1.1153 \cdot 10^{-4}$ **Max torque** $2.4555 \cdot 10^{-6}$ Nm **Min torque** $-2.4555 \cdot 10^{-6}$ Nm	**Cost function** $1.1561 \cdot 10^{-4}$ **Max torque** $1.2080 \cdot 10^{-6}$ Nm **Min torque** $-1.2080 \cdot 10^{-6}$ Nm	**Cost function** $1.2356 \cdot 10^{-4}$ **Max torque** $7.0086 \cdot 10^{-7}$ Nm **Min torque** $-7.0086 \cdot 10^{-7}$ Nm
10°	**Cost function** $1.5039 \cdot 10^{-4}$ **Max torque** $6.2295 \cdot 10^{-6}$ Nm **Min torque** $-6.2295 \cdot 10^{-6}$ Nm	**Cost function** $1.4485 \cdot 10^{-4}$ **Max torque** $3.2725 \cdot 10^{-6}$ Nm **Min torque** $-3.2725 \cdot 10^{-6}$ Nm	**Cost function** $1.4705 \cdot 10^{-4}$ **Max torque** $1.9906 \cdot 10^{-6}$ Nm **Min torque** $-1.9906 \cdot 10^{-6}$ Nm
15°	**Cost function** $1.8906 \cdot 10^{-4}$ **Max torque** $1.0087 \cdot 10^{-5}$ Nm **Min torque** $-1.0087 \cdot 10^{-5}$ Nm	**Cost function** $1.7387 \cdot 10^{-4}$ **Max torque** $5.4732 \cdot 10^{-6}$ Nm **Min torque** $-5.4732 \cdot 10^{-6}$ Nm	**Cost function** $1.7015 \cdot 10^{-4}$ **Max torque** $3.4342 \cdot 10^{-6}$ Nm **Min torque** $-3.4342 \cdot 10^{-6}$ Nm

Table 5.7: Cost function (i.e. integral of $|u|$) and maximum and minimum applied torque values for a field-of-view rotation manoeuvre of 5, 10 and 15 degrees about the x-axis in 15, 20 and 25 minutes, considering the CubeSat configuration.

Chapter 6

Conclusions

6.1 Discussion

The objective of the present study is to contextualise the utilization of the RAFTER optical instrument in the setting of a space mission devoted to astrometric exoplanet detection. In particular, emphasis is placed on the field of view shift manoeuvres that the spacecraft that would host the instrument on board would have to perform in order to point it at a new target each time and carry out the next round of observations. The reason for this choice lies in the fact that these are among the most interesting nominal attitude manoeuvres from the standpoint of assessing the torques at play during the mission, which can serve as a preliminary basis for the sizing of the actuating system, as well as being among the most characterising of the mission profile since they derive from its specific observation requirements.

The base manoeuvres are modelled and simulated by solving a constrained optimization problem, which takes into account the dynamics and kinematics of the system in the presence of the solar radiation pressure, as well as specific constraints related to pointing requirements and arising from the limits of actuators and sensors. The objective of the optimization is to minimize a cost function associated with the energy required to perform the manoeuvre. Two spacecraft configurations with RAFTER on board are considered, namely a medium-class satellite and a 18U CubeSat. The optimization is carried out employing two selected cost functions: the integral over time of the square of the input torque and integral over time of the absolute value of the input torque. Subsequent simulations vary the manoeuvring conditions, i.e. axis of rotation, angle of rotation, duration of the manoeuvre, method of solution to the optimization problem and maximum allowable control torque, to assess the impact of these adjustments on the outcomes achieved.

The results demonstrate that the control torques necessary for the successful completion of the manoeuvres are generally within the range of $10^{-4}/10^{-3}$ Nm for the nominal configuration and $10^{-7}/10^{-6}$ Nm for the CubeSat configuration. Such values represent a significant first clue as to the feasibility of the mission on an energetic level, as well as an additional tool for a preliminary selection of the actuating system of the spacecraft.

For the nominal configuration, optimization of u^2 typically yields continuous torques with a linear behaviour that can approximate those delivered by a reaction wheel system. Conversely, optimization of $|u|$ often results in torques supplied exclusively at the beginning and end of the manoeuvre, in a sort of *bang-bang* fashion, akin to those obtained by operating a set of thrusters. In the latter case, the order of magnitude of the maximum allowable torque determines whether the observed torque will exhibit quasi-impulsive behaviour and a greater magnitude than that attained by optimizing u^2, or a lower

maximum value equal to that of the maximum allowable torque, which is delivered for a longer time at the beginning and end of the manoeuvre. In the case of the CubeSat configuration, the general discourse remains essentially unchanged. However, an unusual behaviour is observed when optimising u^2 with a maximum allowable torque greater than 10^{-6} Nm, which is more similar to what one would expect to achieve when optimising |u| instead. It also exhibits torque fluctuations around zero during the central phase of the manoeuvre, during which the satellite orients itself towards the desired attitude. This behaviour may warrant further investigation.

The work presented in this thesis has resulted in a paper that will be published in the SPIE proceedings of the Ground-based and Airborne Telescopes X conference, held as part of the SPIE Astronomical Telescope + Instrumentation 2024.[50]

6.2 Future work

The work presented in this thesis provides a preliminary foundation for a comprehensive investigation into a potential mission that could satisfy the purpose for which RAFTER was conceived, namely conducting localized astrometric observations from space with the aim of detecting the presence of exoplanets. Said mission profile can be further investigated by, for example, undertaking a more detailed study of mission operations or, rather, by delineating in greater depth the potential spacecraft employed and its systems, starting with the actuating one. The values obtained in this study can in fact not only offer an estimate of the order of magnitude of the input torques required to perform basic pointing manoeuvres, but also stand as a starting point and a characterizing requirement for future actuator sizing.

Furthermore, the mathematical model itself adopted in this study could subsequently be updated to more closely align with a real-world scenario, for instance by taking into account a more accurate representation of solar radiation pressure contribution. A parameterisation could be performed by considering a larger number of conditions to be evaluated, or by adjusting the optimisation method, for example by contemplating the use of indirect methods to solve the constrained optimization problem.

Finally, there are a multitude of aspects that, remaining purely within the domain of mission operations and flight mechanics, can be explored in greater depth in the future, such as the study of maintaining pointing stability throughout each observation, which is fundamental given the high accuracy required for relatively long periods of time to achieve an effective performance, or rather focusing on orbit correction manoeuvres, for instance those carried out during the station-keeping phases.

Bibliography

[1] Morgan-keenan spectral classification. https://en.wikipedia.org/wiki/File:Morgan-Keenan_spectral_classification.svg, visited on 12 July 2024.

[2] Mahima Kaushik, Aditee Mattoo, and Ritesh Rastogi. Exoplanet detection: A detailed analysis, 2024.

[3] Catalog page for pia2125. https://photojournal.jpl.nasa.gov/catalog/PIA21425, visited on 13 July 2024.

[4] Detecting exoplanets with radial velocity. https://www.esa.int/ESA_Multimedia/Images/2019/02/Detecting_exoplanets_with_radial_velocity, visited on 15 July 2024.

[5] Debra A. Fischer, Andrew W. Howard, Greg P. Laughlin, Bruce Macintosh, Suvrath Mahadevan, Johannes Sahlmann, and Jennifer C. Yee. Exoplanet detection techniques. *Protostars and Planets VI*, 2015.

[6] Exoplanet caught on the move. https://www.eso.org/public/images/eso1024a/, visited on 13 July 2024.

[7] Astrometry and gaia. http://spiff.rit.edu/classes/resceu/lectures/astrom/astrom.html, visited on 14 July 2024.

[8] Very large telescope. https://www.britannica.com/topic/Very-Large-Telescope, visited on 14 July 2024.

[9] Gaia's sky in colour. https://sci.esa.int/web/gaia/-/60169-gaia-s-sky-in-colour, visited on 14 July 2024.

[10] Mario Gai, Alberto Vecchiato, Alberto Riva, Alexey G. Butkevich, Deborah Busonero, Zhaoxiang Qi, and Mario Gilberto Lattanzi. Relative astrometry in an annular field. *Publications of the Astronomical Society of the Pacific*, 2022.

[11] Alberto Riva, Mario Gai, Alberto Vecchiato, Deborah Busonero, Mario Gilberto Lattanzi, Federico Landini, Zhaoxiang Qi, and Zhenghong Tang. Rafter: Ring astrometric field telescope for exo-planets and relativity. In *Space Telescopes and Instrumentation 2020: Optical, Infrared, and Millimeter Wave*, volume 11443 of *Proc. SPIE*, 2020.

[12] Aleš Janota, Vojtech Šimák, Dušan Nemec, and Jozef Hrbček. Improving the precision and speed of euler angles computation from low-cost rotation sensor data. *Sensors*, 2015.

[13] Matthew P. Kelly. An introduction to trajectory optimization: How to do your own direct collocation. *SIAM Review*, 2017.

[14] Euclid | ipac. https://www.ipac.caltech.edu/project/euclid, visited on 21 May 2024.

[15] 12u platform on satsearch. https://satsearch.co/products/c3s-12u-platform, visited on 21 May 2024.

[16] Euclid Collaboration. The euclid wide survey. *Astronomy and Astrophysics*, 2022.

[17] Changqing Wu and Xiaodong Han. Energy-optimal spacecraft attitude maneuver path-planning under complex constraints. *Acta Astronautica*, 2019.

[18] G. F. Benedict, B. E. McArthur, T. Forveille, X. Delfosse, E. Nelan, R. P. Butler, W. Spiesman, G. Marcy, B. Goldman, C. Perrier, W. H. Jefferys, and M. Mayor. A Mass for the Extrasolar Planet Gliese 876b Determined from Hubble Space Telescope Fine Guidance Sensor 3 Astrometry and High-Precision Radial Velocities. *The Astrophysical Journal*, 2002.

[19] Detecting exoplanets with astrometry. https://sci.esa.int/web/gaia/-/58788-detecting-exoplanets-with-astrometry, visited on 22 May 2024.

[20] Fabien Malbet et al. Faint objects in motion: The new frontier of high precision astrometry. *Experimental Astronomy, 51(3)*, 2021.

[21] Arnaud Cassan et al. One or more bound planets per milky way star from microlensing observations. *Nature*, 2012.

[22] Erik A. Petigura, Andrew W. Howard, and Geoffrey W. Marcya. Prevalence of earth-size planets orbiting sun-like stars. In *Proceedings of the National Academy of Sciences of the United States of America*, volume 110, 2013.

[23] Xavier Bonfils, Thierry Forveille, Xavier Delfosse, Stéphane Udry, Michel Mayor, Christian Perrier, François Bouchy, Francesco Pepe, Didier Queloz, and Jean-Loup Bertaux. The harps search for southern extra-solar planets. vi. a neptune-mass planet around the nearby m dwarf gl 581. *Astronomy and Astrophysics*, 2005.

[24] Eric E. Mamajek et al. Initial conditions of planet formation: Lifetimes of primordial disks. In *AIP Conference Proceedings*, volume 1158, 2009.

[25] W.K.M. Rice and Philip J. Armitage. On the formation time scale and core masses of gas giant planets. *The Astrophysical Journal*, 2003.

[26] Nuria Calvet, Paola D'Alessio, Lee Hartmann, David Wilner, Andrew Walsh, and Michael Sitko. Evidence for a developing gap in a 10 myr old protoplanetary disk. *The Astrophysical Journal*, 2002.

[27] Malcolm Fridlund et al. Epic 210894022b - a short period super-earth transiting a metal poor, evolved old star. *Astronomy and Astrophysics*, 2017.

[28] Marc Ollivier and Marie-Christine Maurel. Planetary environments and origins of life: How to reinvent the study of origins of life on the earth and life in the universe under the light of exoplanetology progress. In *BIO Web of Conferences*, volume 2, 2014.

[29] Oxygen is not definitive evidence of life on extra-solar planets. https://astrobiology.com/2015/09/oxygen-is-not-definitive-evidence-of-life-on-extrasolar-planets.html, visited on 15 July 2024.

[30] Ravi Kumar Kopparapu. A revised estimate of the occurrence rate of terrestrial planets in the habitable zones around kepler m-dwarfs. *The Astrophysical Journal Letters*, 2013.

[31] Yutaka Abe, Ayako Abe-Ouchi, Norman H. Sleep, and Kevin J. Zahnle. Habitable zone limits for dry planets. *Astrobiology*, 2011.

[32] Sara Seager. Exoplanet habitability. *Science*, 2013.

[33] 5 ways to find a planet. `https://exoplanets.nasa.gov/alien-worlds/ways-to-find-a-planet/?intent=021#/2`, visited on 14 July 2024.

[34] Jason Wright and B. Gaudi. Exoplanet detection methods. *Planets, Stars and Stellar Systems. Volume 3: Solar and Stellar Planetary Systems*, 2012.

[35] Curvas de luz de los siete planetas de trappist-1 durante su tránsito. `https://www.eso.org/public/chile/images/eso1706h/`, visited on 13 July 2024.

[36] Lucy-Ann McFadden, Paul R. Weissman, and Torrence V. Johnson. *Encyclopedia of the Solar System, 2nd edition.* Elsevier, 2007.

[37] Lennart Lindegren and Dainis Dravins. The fundamental definition of "radial velocity". *Astronomy Astrophysics*, 2003.

[38] F. Pepe, C. Lovis, D. Segransan, W. Benz, F. Bouchy, X. Dumusque, M. Mayor, D. Queloz, N. C. Santos, and S. Udry. The harps search for earth-like planets in the habitable zone. *Astronomy Astrophysics*, 2011.

[39] Sjur Refsdal and Hermann Bondi. The gravitational lens effect. *Monthly Notices of the Royal Astronomical Society*, 1964.

[40] Michael Perryman. *The Exoplanet Handbook.* Cambridge University Press, 2018.

[41] Eso very large telescope. `https://www.eso.org/public/teles-instr/paranal-observatory/vlt/?lang`, visited on 14 July 2024.

[42] Elt | eso. `https://elt.eso.org/`, visited on 14 July 2024.

[43] Planetary systems on nasa exoplanet archive. `https://exoplanetarchive.ipac.caltech.edu/cgi-bin/TblView/nph-tblView?app=ExoTbls&config=PS&constraint=default_flag%3E0&constraint=disc_method%20like%20%27%25ast%25%27`, visited on 14 July 2024.

[44] Gaia data release documentation: Astrometric precision and accuracy. `https://gea.esac.esa.int/archive/documentation/GDR2/Catalogue_consolidation/chap_cu9val_cu9val/sec_cu9val_944/ssec_cu9val_944_wp944astrometry.html`, visited on 14 July 2024.

[45] Toliman space telescope. `https://toliman.space/`, visited on 14 July 2024.

[46] Giulio Avanzini. Notes of the course 'spacecraft attitude dynamics and control'. Technical report, Politecnico di Torino, 2009.

[47] Elisa Capello. Slides of the course 'spacecraft dynamics and control'. Technical report, Politecnico di Torino, 2022.

[48] Matthew P. Kelly. *OptimTraj Users Guide.*

[49] J.R. Wertz and Wiley J. Larson. *Space Mission Analysis and Design.* Springer Dordrecht, 1999.

[50] Chiara Scandaglia, Alberto Riva, Lorenzo Casalino, Deborah Busonero, Mario Gai, and Alberto Vecchiato. Study and analysis of pointing manoeuvres for the rafter mission. Accepted, in press, 2024.